



ISLAMIC UNIVERSITY OF TECHNOLOGY
ORGANISATION OF ISLAMIC COOPERATION



**EFFECT OF VARIATION OF AERODYNAMIC BRAKE PLATE
ORIENTATION AND MULTIPLE BRAKE GEOMETRIES ON
INCIDENT DRAG OF HYPERLOOP POD**

BACHELOR OF SCIENCE IN MECHANICAL ENGINEERING

Authored by

SHAHNOOR SHAMIM KHAN

Student ID: 151405

SHADMAN MAHMUD

Student ID: 151412

ADIB ADNAN

Student ID: 151443

Supervised by

PROF. DR. MD. HAMIDUR RAHMAN

DEPARTMENT OF MECHANICAL AND PRODUCTION ENGINEERING

Islamic University of Technology

NOVEMBER 2019

CERTIFICATE OF RESEARCH

The thesis titled “Effect of Variation of Aerodynamic Brake Plate Orientation and Multiple Brake Geometries on Incident Drag of Hyperloop Pod” submitted by Shahnour Shamim Khan (151405), Shadman Mahmud (151412) and Adib Adnan (151443) has been accepted as satisfactory in partial fulfillment of the requirement for the Degree of Bachelor of Science in Mechanical Engineering.

Supervisor

Prof. Dr. Md. Hamidur Rahman

Department of Mechanical and Production Engineering (MPE)

Islamic University of Technology (IUT)

Head of the Department

Prof. Dr. Md. Zahid Hossain

Department of Mechanical and Production Engineering (MPE)

Islamic University of Technology (IUT)

DECLARATION

We hereby declare that this thesis titled “Effect of Variation of Aerodynamic Brake Plate Orientation and Multiple Brake Geometries on Incident Drag of Hyperloop Pod” is an authentic report of our study carried out as requirement for the award of degree B.Sc. (Mechanical Engineering) at Islamic University of Technology, Gazipur, Dhaka, under the supervision of Prof. Dr. Md. Hamidur Rahman, MPE, IUT during January 2019 to November 2019.

The matter embodied in this thesis has not been submitted in part or full to any other institute for award of any degree.

Shahnoor Shamim Khan

Student no. 151405

Shadman Mahmud

Student no. 151412

Adib Adnan

Student no. 151443

This is to certify that the above statement made by the students concerned is correct to the best of my knowledge and belief.

Prof. Dr. Md. Hamidur Rahman

Department of Mechanical and Production Engineering (MPE)

Islamic University of Technology

Acknowledgments

Foremost, we would like to express our sincere gratitude to our advisor Prof. Dr. Md. Hamidur Rahman for the continuous support of our undergraduate study and research, for his patience, motivation, enthusiasm, and immense knowledge. His guidance helped us throughout the span of our research and eventually writing of this thesis.

Besides our advisor, we would also like to thank respected Sayedus Salehin Sir, Tahsin Sejat Saniat Sir, Mohammed Raihan Uddin Sir, and Rezwanul Karim Sir for their encouragement, insightful comments, and constructive questions. This work would not be possible without their support.

Table of Contents

Nomenclature	viii
Abstract	ix
Chapter 1 Introduction	1
Chapter 2 Governing Theories	5
2.1 Steady Flow	5
2.2 Turbulent Flow	5
2.3 The No-Slip Condition	5
2.4 The Free-Slip Condition	6
2.5 The Boundary Layer	6
2.6 Boundary Layer Separation	7
2.7 Drag	7
2.8 Lift	8
2.9 Continuum	8
2.10 The Knudsen Number	8
2.11 Compressibility	9
2.12 Subsonic Flow	10
2.13 Governing Equations	11
2.13.1 Continuity Equation.....	11
2.13.2 Navier-Stokes Equation	11
2.13.3 Conservation of Energy Equation	12
2.13.4 Reynolds Averaged Navier-Stokes Equations.....	12
2.15 Turbulence Model	13
2.16 $k - \omega$ SST Turbulence Model	13
2.17 Test Domain Discretization	15
2.18 Kantrowitz Limit and Choked Flow.....	15
Chapter 3 Numerical Methodology	17
3.1 System Modelling.....	17
3.2 Variation of Brake Angle of Attack	19
3.2.1 Constant Brake Plate Length	21
3.2.2 Constant Brake Profile Length	22
3.3 Multiple or Split Brakes	22

3.4 Computational Grid Quantization	25
3.5 Mesh Quality and Grid Independence	25
3.6 Boundary Conditions.....	28
3.7 Validation	29
Chapter 4 Results for Angled Brakes.....	31
Chapter 5 Results for Multiple or Split Brakes	59
5.1 Three Brakes of Equal Length.....	59
5.2 Two Brakes of Different Lengths.....	61
5.3 Two Brakes of Equal Length.....	62
Chapter 6 Conclusions and Scope of Further Work	65
Bibliography	67

Nomenclature

T = Temperature

P = Pressure

ρ = Density

A = Area

V or v = Velocity

c = Speed of sound

Ma = Mach number

R = Gas constant

λ = Mean free path

k_b = Boltzmann constant

d = Molecular diameter

l = Characteristic length

\dot{m} = Mass flow rate

γ = Specific heat ratio

τ = Shear stress

σ = Normal stress

μ = Dynamic viscosity

μ_t = Eddy viscosity

C_D = Drag coefficient

T_t = Temperature at throat

P_t = Pressure at throat

t = Time

x, y, z = Cartesian coordinates

u = Velocity component in x-direction

v = Velocity component in y-direction

w = Velocity component in z-direction

h = Specific enthalpy

k = Turbulent kinetic energy

ω = Turbulence frequency

S = Rate of deformation

δ_{ij} = Kronecker delta

Abstract

The idea for the Hyperloop has received significant attention, with commentators and analysts expecting it to become a revolutionary and potentially the fastest mode of land transportation on the planet. Various companies and multiple universities are involved in the development of this new system and in combatting the myriad of design challenges that it poses. Of particular interest in academic circles has been the optimization of the pod geometry and fluid flow regime for the functioning of the Hyperloop pod in the low-pressure environment. Multiple studies have been carried out using numerical simulations to obtain insights into the different factors affecting the Hyperloop's performance. The low-pressure tube through which the Hyperloop pod travels, presents a case that has not been faced in other transport models. The Hyperloop pod is expected to travel at speeds close to Mach 1.0, and as such acceleration and deceleration of the pod is of critical importance if passenger safety protocols are to be maintained. The high-speed flow around the pod exerts high adverse pressure gradients on the pod surface, resulting in boundary layer separation, increasing drag and affecting the acceleration of the pod and requiring greater power. Numerical simulations have shown that the placement of an aerodynamic brake plate on the pod surface at the point at which boundary layer separation occurs in the low-pressure region provides the necessary drag required for safe deceleration, as well as provide the required downforce to counteract the lift forces, which become significant due to the low-pressure regions above the pod, enabling the pod to stay on the track. This study was aimed to find the best angle for the aerodynamic brake plate positioned at a fixed point of 0.24 of the chord length of the pod, allowing for the maximum generation of drag, using numerical simulations. After various trials, it was observed that placing the plate normal to the flow produced the highest drag, with one exception –when angling the plate backwards while increasing its length to keep incident brake profile constant, the drag at first increased slightly and then decreased. This study also studied another design feature, one involving the brake plate split and placed at different chord lengths of the pod.

Keywords: aerodynamics, CFD, compressible flow, fluid mechanics, high speed transport, numerical analysis, turbulence.

Chapter 1

Introduction

With the growth of the global workforce, as well as the rapid industrialization of urban areas worldwide, the demand for safe and fast transportation systems has reached peak levels. Consequently, the proposal of the Hyperloop concept by Elon Musk in 2013 was aimed to solve this problem, with the publication of the white paper [1] receiving great attention from both academic circles and the general public.

The concept of the Hyperloop is very innovative in its approach: a pod carrying passengers or cargo travels through a tube at reduced pressure. The pod levitates above the track, by action of air bearings or magnetic levitation. If air bearing system is used, a compressor may be placed at the front of the pod to intake the required air.



Figure 1.1 Concept pod of Hyperloop Transportation Technologies [24]

Due to the reduced pressure and friction due to pod levitation, the drag encountered by the pod is significantly reduced, and as a result, the tube is expected to be able to move at relatively high Mach number speeds, around 0.7 Ma. Consequently, the travel times between destinations reduces drastically, with the expected time for travelling between Los Angeles and San Francisco, a distance of 560 kilometers, becoming 35 minutes. This is a large decrease in commute time, compared to the 57 minutes of commute by air, and the projected 158 minutes by the California High Speed Rail [1]. The Hyperloop is thus able to drastically reduce travel times between cities where

travelling by cars would take hours and air travel would involve multiple hours wasted in airport commute, immigration lines and boarding.

In the initial Hyperloop Alpha white paper published by Musk through SpaceX, it was proposed that the pod would be travelling in a partial vacuum tube, with pressures of 100 Pa, reaching speeds of up to 700 mph or 1200 km/h, almost on the brink of Mach 1. Due to the inherent inefficiencies and friction forces that wheels and a track would introduce at such speeds, a system of air bearing was proposed that would allow the pod to levitate above the track. The linear thrust and propulsion of the pod was to be carried out by linear induction motors [1].

As the concept was completely new and lacking any previous research, the white paper was published for free and the concept deemed an open source idea. These decisions have helped foster research and innovation regarding the Hyperloop and there has been significant work done in academic circles, such as that by Braun et al [2], Chin et al [4] and Opgenoord and Caplan [3]. These works have also highlighted the shortcomings in the initial proposal, as well as offering more pragmatic alternatives. For example, it was shown by Chin et al [4] that for the pod to reach Mach 0.8, the diameter of the tube has to be approximately twice the diameter specified in the original white paper, otherwise the flow would be subject to choking due to lower bypass annular area for the air. Similarly, Opgenoord and Caplan [3] and the MIT Hyperloop Team [18] showed that the use of a compressor and air bearing system is less energy efficient compared to the use of a highly aerodynamic design and magnetic levitation.

Significant work on the pod aerodynamics and the design analysis were carried out by Braun et al [2]. The work involved the use of a computational approach, setting up a pod travelling in a tube and studying the motion in a section of the tube, with the primary objective being the maximization of aerodynamic lift force in order to reduce required work input for pod levitation. While initially wanting to optimize the aerodynamic design for lift, significant insights were also gained regarding the drag reduction for the design. Since maintaining pressures of 100 Pa is too difficult a task and not feasible from an economic perspective, Braun et al [2] conducted the study by keeping tube pressure at about 10% of atmospheric level, i.e. 11000 Pa. This is in

accordance with the work done by Opgenoord and Caplan [3], who showed that below this level, the decrease in drag forces becomes relatively insignificant. Braun et al presented the various pressure regions around the pod surface, how the Mach numbers changed as the air flowed around the pod. The creation of the low-pressure regions above the pod surface and hence, the separation of boundary layer came to light. The low-pressure region above the pod surface also resulted in a significant lift force being exerted on the pod. The phenomena of boundary layer separation increased the drag forces on the pod.

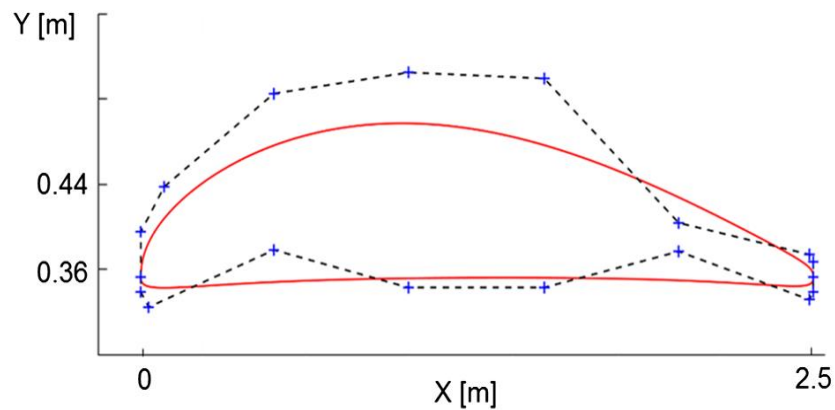


Figure 1.2 Braun’s representation of Bezier parameterization for initial design [2]

Subsequent work was done by Saniat and Raihan [28], who used a similar computational approach to analyze the introduction and effectiveness of an aerodynamic brake plate on the pod surface to maintain a necessary amount of drag and produce the required downforce to combat the lift generated. Studies were done with the brake plate at inclination angles of 30°, 45°, 60° and 90° with the plate at 90° generating the optimum drag and downforce.

To facilitate and encourage research, SpaceX also announced the Hyperloop Pod Competition in 2015 for universities [19]. The competition has a mile-long test track at SpaceX Headquarters, Hawthorne, California with an accelerator assistant and levitation panel and the tube capable of maintaining varying internal pressures so that multiple designs of the pod can be run in search of the best pod shape. The first two editions of the competition, held in January 2017 and August 2017, were both won by WARR Hyperloop from Technical University of Munich. The third edition held in July 2018 was again won by WARR Hyperloop with the pod reaching a record speed

of 457 kmph or 284 mph [20]. The latest edition of the competition held in July 2019 had WARR Hyperloop breaking their previous speed record to reach 464 kmph or 288 mph [21].



Figure 1.3 Contest pod travelling through the test tube [22]

While the Hyperloop project is making strides globally with its first 10 km stretch set to open by 2020 in the UAE and developments in the US, China and parts of Europe progressing, India might become the frontrunner to build the first Hyperloop. The proposed link connecting Mumbai and Pune will slash the current 3.5 hours travel time to under 35 minutes.

Chapter 2

Governing Theories

The study of the hyperloop presents certain unique features in its physics and its behavior along with the fundamental flow characteristics. This chapter provides a comprehensive insight into these theories and how they might influence the behavior of the various design angles of the aerodynamic braking system for the hyperloop pod.

2.1 Steady Flow

The term ‘steady’ implies ‘no change of properties at a specific point with time’. For a flow, if the fluid properties at any fixed location does not change with time, this flow is defined to be a steady flow.

2.2 Turbulent Flow

A fluid flow which is highly disordered and is characterized by velocity fluctuations is called ‘turbulent flow’. Turbulent flows typically occur at high velocities. Since air is a low-viscosity fluid having a dynamic viscosity of 1.895×10^{-5} kg/m-s at 35°C [10], the flow of air at high velocities results in a turbulent flow.

2.3 The No-Slip Condition

The no-slip condition implies that a fluid in direct contact with a surface sticks to the surface and there is no slip. This means that the normal and tangential velocity components of the fluid at the surface is zero. The fluid property responsible for the no-slip condition is viscosity. This phenomenon also gives rise to the boundary layer.

2.4 The Free-Slip Condition

The free slip boundary condition is equivalent to the absence of tangential shear stress along the boundary. The free-slip boundary condition says that at the interface between a moving fluid and a stationary wall, the normal component of the fluid velocity field is equal to zero, but the tangential component is unrestricted.

2.5 The Boundary Layer

The boundary layer is a result of the no-slip condition. During flow over a surface, the layer that sticks to the surface slows the adjacent fluid layer because of viscous forces between the fluid layers, which slows the next layer, and so on. Hence, when a vertical line is considered on any point on the surface, the fluid velocity is different on every point on the line, up to a certain distance from the surface. This flow region adjacent to the wall, in which the viscous effects (and thus the velocity gradients) are significant, is called the boundary layer.

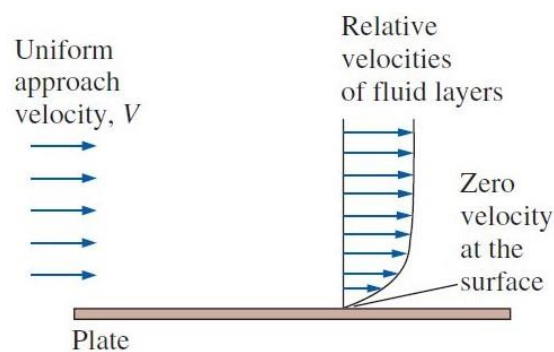


Figure 2.1 Development of a boundary layer [10]

Because of the no-slip condition, shear friction occurs at the surface which is in contact with the fluid. This friction slows down the moving object (in this case, the pod). This drag is known as skin friction drag.

Within the boundary layer region, the viscous effects of the fluid become dominant whereas its influence become less pronounced in the free stream region outside the boundary layer. As such, it is essential to treat the fluid near the surface differently. In numerical simulation it is very important to properly capture this boundary layer to

accurately predict the fluid flow and skin friction. This is done by discretizing the flow field, which is discussed in detail in the following sections.

2.6 Boundary Layer Separation

Most flows encountered have a favorable pressure gradient, which means that the pressure is higher at the upstream and lower at the downstream. This pressure gradient helps to accelerate the flow. However, the flow velocity is still zero at the surface due to the no-slip condition and gradually increases in the flow direction as we go up through the boundary layer.

On the other hand, there can be flows that occur against an adverse pressure gradient, where the downstream pressure is higher than the upstream pressure. Such a pressure gradient opposes the fluid flow. Since the flow velocity is zero at the surface, there is a possibility of some flow occurring in the reverse direction close to the surface, provided that the adverse pressure gradient is strong enough. This leads to the boundary layer developing a point of inflection, known as ‘boundary layer separation’.

Boundary layer separation results in a wake region just downstream of the point of inflection where recirculation occurs, thereby changing the flow characteristics.

2.7 Drag

Every object meets some resistance when it is forced to move through a fluid. The force a fluid exerts on a moving body opposite to the body’s direction of motion is called drag. The amount of drag can be calculated from [10] –

$$F_D = C_D \frac{1}{2} \rho V^2 A \quad (2.1)$$

There are two types of drag – (i) Pressure drag and (ii) Skin friction drag.

The part of the drag that is due directly to pressure is called pressure drag. Pressure drag is most prominent in flows around blunt bodies such as vertical plates, cylinders,

spheres, etc. and is negligible for flows around streamlined bodies such as horizontal plates, aircraft wings etc. For the Hyperloop brake plate, the pressure drag will be the main contributor to the braking force.

The reverse is true for skin friction drag. The part of the drag that is due directly to the wall shear stress is called skin friction drag.

2.8 Lift

In addition to drag, a moving body in a fluid experiences lift. Lift is the summation of the components of pressure and wall shear forces in the direction normal to the flow and tends to move the body in that direction.

2.9 Continuum

Every fluid is composed of molecules which may be closely situated or widely spaced apart, the latter usually being the case with gases. Yet it is convenient to disregard the atomic nature of the fluid and view it as a continuous, homogeneous matter with no holes, that is, a continuum. The continuum idealization allows for the treatment of properties as point functions and to assume that the properties vary continually in space with no jump discontinuities. This idealization is valid as long as the size of the system in question is large relative to the space between the molecules. Molecular density, characterized by mean free path (λ), is one of the important factors which dictate the validity of the continuum assumption of fluid. If the mean free path is very insignificant in comparison to the characteristic length then the continuum assumption is valid.

2.10 The Knudsen Number

The Knudsen number (Kn) is a dimensionless number defined as the ratio of the molecular mean free path length to a representative physical length scale.

$$Kn = \frac{\text{Mean free path length}}{\text{Characteristic length}} = \frac{\lambda}{L} = \frac{k_b T}{\sqrt{2}\pi d^2 P l} \quad (2.2)$$

The Knudsen Number is used to determine whether continuum mechanics or statistical mechanics is to be used to model a fluid flow [14]. If $Kn < 0.01$, continuum assumption is valid.

The validity of the continuum approach has already been presented for the Hyperloop pod operating at pressure as low as 100 Pa [8] and the dimensionless Knudsen number is shown to be less than 0.01 for the flow regime. Thus, the continuum approach is valid for further analysis [2].

2.11 Compressibility

A flow is said to be incompressible if the density remains nearly constant throughout. On the other hand, a flow in which significant density changes occur is called a compressible flow.

Whether a flow is compressible or incompressible is determined by the Mach number of the flow. The Mach is defined as the ratio of the flow velocity to the speed of sound.

$$Ma = \frac{v}{c} = \frac{v}{\sqrt{\gamma RT}} \quad (2.3)$$

If $Ma < 0.3$, then the flow is considered incompressible. The density change associated with such flows is less than 5% of the initial density.

In our case, the maximum observed Mach number at the symmetry plane is close to 0.78, well over the threshold value of 0.3 and hence, compressibility effects need to be taken into account.

The isentropic compressible equations are used to validate the results of the simulation in simple cases such as the case without the brake. The mass flow rate of such instance is given by the equation [10] –

$$\dot{m} = \frac{P_t}{\sqrt{RT_t}} A \sqrt{\gamma} Ma \left(1 + \frac{\gamma - 1}{2} Ma^2\right)^{\frac{\gamma + 1}{2 - 2\gamma}} \quad (2.4)$$

Since, the mass is conserved at all sections of the pod, this mass flow rate can be used to calculate the Mach number at different sections of the pod once the area ratio is known.

From this Mach number we can calculate various other flow properties like temperature, pressure, density respectively at that specific section of the pod by the following relations:

$$\frac{T_t}{T} = 1 + \frac{\gamma - 1}{2} Ma^2 \quad (2.5)$$

$$\frac{P_t}{P} = \left(1 + \frac{\gamma - 1}{2} Ma^2\right)^{\frac{\gamma}{\gamma - 1}} \quad (2.6)$$

$$\frac{\rho_t}{\rho} = \left(1 + \frac{\gamma - 1}{2} Ma^2\right)^{\frac{1}{\gamma - 1}} \quad (2.7)$$

This analysis assumes the flow to be simple, isentropic and one dimensional thus can be termed as a ‘reduced model’. There is a maximum difference of 5% between the results obtained from simulations and the results from the reduced model which is further discussed in the validation section.

2.12 Subsonic Flow

Fluid flows can be categorized into subsonic, sonic or supersonic based on the Mach number. For $Ma < 1.0$, the flow is subsonic. As mentioned earlier, our maximum observed Mach number is 0.78 and therefore the flow is subsonic. It is essential that the flow remains subsonic throughout the entire domain so as not to give rise to the possibility of shock occurring anywhere in the flow.

2.13 Governing Equations

The fundamental equations that govern fluid flow are simultaneously solved to obtain the temperature, pressure and velocity at specific points in a flow field. These equations are discussed below.

2.13.1 Continuity Equation

The continuity equation basically states that the rate of change of mass in a fluid flow is zero, that it is conserved. If a control volume is considered anywhere in the flow field, then, according to the continuity equation, the mass flow into the control volume would be equal to the mass flow out of the control volume. The equation is given as [10] –

$$\frac{\partial \rho}{\partial t} + \vec{\nabla} \cdot (\rho \vec{V}) = 0 \quad (2.8)$$

Here, $\frac{\partial \rho}{\partial t}$ is the time rate of change of density.

2.13.2 Navier-Stokes Equation

The Navier-Stokes equation in x, y, z directions respectively can be expressed as [13]

–

$$\frac{\partial(\rho u)}{\partial t} + \nabla \cdot (\rho u \vec{V}) = -\frac{\partial P}{\partial x} + \frac{\partial \tau_{xx}}{\partial x} + \frac{\partial \tau_{yx}}{\partial y} + \frac{\partial \tau_{zx}}{\partial z} + \rho f_x \quad (2.9)$$

$$\frac{\partial(\rho v)}{\partial t} + \nabla \cdot (\rho v \vec{V}) = -\frac{\partial P}{\partial y} + \frac{\partial \tau_{xy}}{\partial x} + \frac{\partial \tau_{yy}}{\partial y} + \frac{\partial \tau_{zy}}{\partial z} + \rho f_y \quad (2.10)$$

$$\frac{\partial(\rho w)}{\partial t} + \nabla \cdot (\rho w \vec{V}) = -\frac{\partial P}{\partial z} + \frac{\partial \tau_{xz}}{\partial x} + \frac{\partial \tau_{yz}}{\partial y} + \frac{\partial \tau_{zz}}{\partial z} + \rho f_z \quad (2.11)$$

The quantities on the left-hand side of the equation denote the rate of change of momentum in the x, y, z directions. The acceleration of the fluid element is presented as a summation of the local acceleration and the convective acceleration. The

quantities on the right-hand side of the equation denote the summation of different forces acting on a per unit area and volume basis. Hence it is basically a modified form of Newton's 2nd law of motion.

2.13.3 Conservation of Energy Equation

The compact form of the conservation of energy can be written as [13] –

$$\rho \frac{D}{Dt} (h) = \frac{D}{Dt} (P) + \nabla \cdot (\nabla \lambda T) \quad (2.12)$$

2.13.4 Reynolds Averaged Navier-Stokes Equations

The Navier-Stokes equations are capable of defining turbulent flows of non-Newtonian fluids. However, it is not a very efficient approach since doing so requires massive computational requirements and time. Hence, an averaging approach known as Reynolds Averaged Navier-Stokes, or RANS for short, is implemented and is termed as the basis of turbulent flows. There are 3 common forms of expressing the Reynolds Averaging –

Time average:

$$F_T(x) = \lim_{x \rightarrow \infty} \frac{1}{T} \int_t^{t+T} f(x, t) dt \quad (2.13)$$

Spatial average:

$$F_v(t) = \lim_{v \rightarrow \infty} \frac{1}{v} \iiint f(x, t) dV \quad (2.14)$$

Ensemble average:

$$F_E(x, t) = \lim_{N \rightarrow \infty} \frac{1}{N} \sum_{n=1}^N f_n(x, t) dV \quad (2.15)$$

For flows that do not vary with time the time averaging approach is used. This is the most commonly encountered form in most engineering applications. The spatial averaging is used for flows having average uniform turbulence in any given direction. The ensemble averaging is suitable for flows decaying with time.

2.15 Turbulence Model

The use of RANS equations introduces 6 unknown variables known as Reynolds stress components which are solved using turbulence models. Turbulence models maybe classified into 3 categories –

- 1) Eddy Viscosity Models
- 2) Reynolds Stress Models
- 3) Direct Numerical Simulation (DES), Large Eddy Simulation (LES), Detached Eddy Simulation (DES)

For this simulation, the 2-equation Eddy Viscosity Model, namely the $k - \omega$ SST Model, has been used.

2.16 $k - \omega$ SST Turbulence Model

The flow in concern is a wall bounded flow and requires the use of a turbulence model that can perform well in the near wall region. Also, the model has to deal with a low Reynold's number flow. So, a low Reynold's turbulence model with good near-wall performance is desirable. The $k - \omega$ Model is a good option in this regard. But it performs poorly in the free stream, away from the wall. The $k - \epsilon$ Model is good for the free stream, but its near-wall performance is unsatisfactory for boundary layers with adverse pressure gradients. This led to the formulation of a hybrid model using

(i) a transformation of the $k - \epsilon$ Model into the $k - \omega$ Model in the near-wall region and (ii) the standard $k - \epsilon$ Model in the fully turbulent region far from the wall. This model is known as the $k - \omega$ Shear Stress Transport (SST) Model.

The Shear Stress Transport (SST) Model accounts for the transport of the turbulent shear stress and gives highly accurate predictions of the onset and the amount of flow separation under adverse pressure gradients. The Eddy Viscosity formulation is modified to account for the transport effects of the principal turbulent shear stress. The transformation from $k - \epsilon$ to $k - \omega$ and vice versa is done by a blending function.

The equations for k and ω are as follows [16] –

$$\frac{\partial(\rho k)}{\partial t} + \text{div}(\rho k U) = \text{div} \left[\left(\mu + \frac{\mu_t}{\sigma_k} \right) \text{grad}(k) \right] + P_k - \beta^* \rho k \omega \quad (2.16)$$

$$\begin{aligned} \frac{\partial(\rho \omega)}{\partial t} + \text{div}(\rho \omega U) &= \text{div} \left[\left(\mu + \frac{\mu_t}{\sigma_{\omega,1}} \right) \text{grad}(\omega) \right] \\ &+ \gamma_2 \left(2\rho S_{ij} \cdot S_{ij} - \frac{2}{3} \rho \omega \frac{\partial U_i}{\partial x_j} \delta_{ij} \right) - \beta_2 \rho \omega^2 \\ &+ 2 \frac{\rho}{\sigma_{\omega,2} \omega} \frac{\partial k}{\partial x_k} \frac{\partial \omega}{\partial x_k} \end{aligned} \quad (2.17)$$

To summarize, the $k - \omega$ SST Model is best suited for –

- Wall bounded boundary layer
- Free shear
- Low Reynold's number flows
- Complex boundary layer flows under adverse pressure gradient and separation (external aerodynamics)

2.17 Test Domain Discretization

Discretization means converting the partial differential equations and the boundary and initial conditions into a system of discrete algebraic equations [12]. The most common discretization methods are – Finite Element Method, Finite Difference Method and Finite Volume Method. ANSYS CFX uses an element based Finite Volume Method. In this method, the test domain is divided into numerous finite volume cells. The cells can be generated by three types of meshing methods – (1) Structured, (2) Unstructured and (3) Hybrid

Unstructured grids are composed of triangular elements (2D) and tetrahedral, prismatic or pyramidal elements (3D). The location of a node cannot be referred to by (i, j, k) indexing.

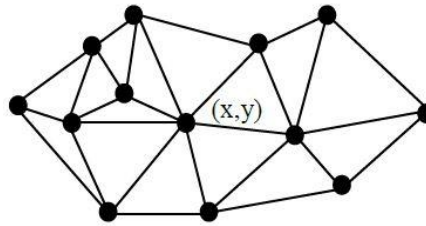


Figure 2.2. Unstructured grid

Unstructured grids can be quickly generated and are good for complex geometries. But it takes relatively longer to achieve convergence.

2.18 Kantrowitz Limit and Choked Flow

Since the Hyperloop pod travels through a tube, the air in front of the pod has to pass through the annulus of the pod and the tube wall. Considering our pod in operation, the annular area gradually decreases from the front up to a certain point and then gradually increases, similar to a converging-diverging nozzle. This imposes two threats.

Firstly, for subsonic flow, the flow velocity increases as the flow area decreases. It is possible that in between the converging and the diverging parts, i.e. the throat, the flow velocity may reach sonic or transonic speeds. Despite the low operating pressure

within the tube, such high velocities will result in considerable amounts of undesired skin friction drag.

Secondly, if the flow velocity were to reach sonic speed at the throat, the following diverging part would allow the flow to become supersonic, since the flow velocity increases as the flow area increases for supersonic flow. This is very much undesirable as there is a chance of shock occurring in this case.

In order to prevent these problems, it is necessary to maintain a minimum area of bypass in the annular region. For subsonic operation, from the isentropic flow equation, it is seen that the ratio of $\frac{Ma_{pod}}{Ma_{bypass}}$ is a function of $\frac{A_{bypass}}{A_{tube}}$, the relation being [4] –

$$\frac{A_{bypass}}{A_{tube}} = \frac{Ma_{pod}}{Ma_{bypass}} \left(\frac{1 + \frac{\gamma-1}{2} Ma_{bypass}^2}{1 + \frac{\gamma-1}{2} Ma_{pod}^2} \right)^{\frac{\gamma+1}{2(1-\gamma)}} \quad (2.18)$$

Chapter 3

Numerical Methodology

3.1 System Modelling

The optimum geometry proposed by Braun et al [2] was taken to be the design on which the various models of the aerodynamic braking system were to be tested. The pod design studied by Braun et al [2] was a scaled down version travelling through a section of the tube. This was done in order to reduce computational power requirement. Figure 3.1 shows the pod travelling through the tube with the boundary walls. The first step in the pod generation was the drawing of the 2D profile of the pod having chord length 2500mm along the symmetrical cross-section plane. The series of points from Braun's base design was projected and then the points were connected by a spline curve. The 2D profile was then extruded 675 mm along the z-axis in order to create the 3D geometry.

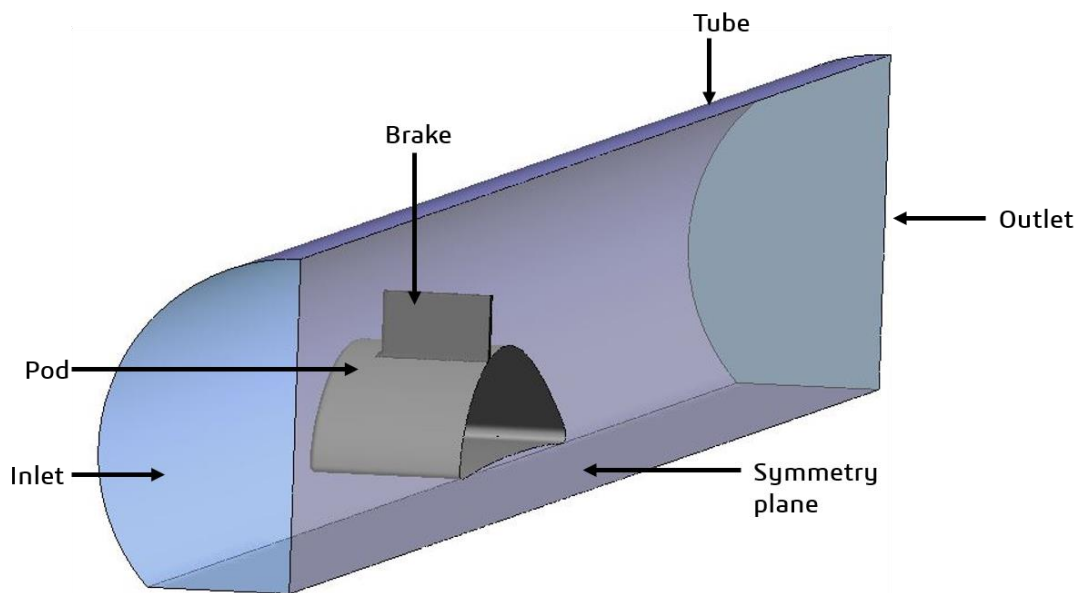


Figure 3.1 3D model of pod with brake plate and boundary conditions

The tube was drawn and generated in accordance with the dimensions specified by SpaceX [17]. The tube diameter was 1810 mm with a concrete base. Due to the concrete base, the pod travels not along a circular tube but along a tube with a flat

track. For the study, the behavior of the pod and the flow physics as it travelled through a section of the tube was investigated and the total tube length was taken to be 14,000 mm. According to Musk [1], the Hyperloop tube would have a constant cross-sectional area and constructed in a straight line with no sharp bends. The pod was centered 4,000 mm from one end of the tub, with this open end being classified as the INLET.

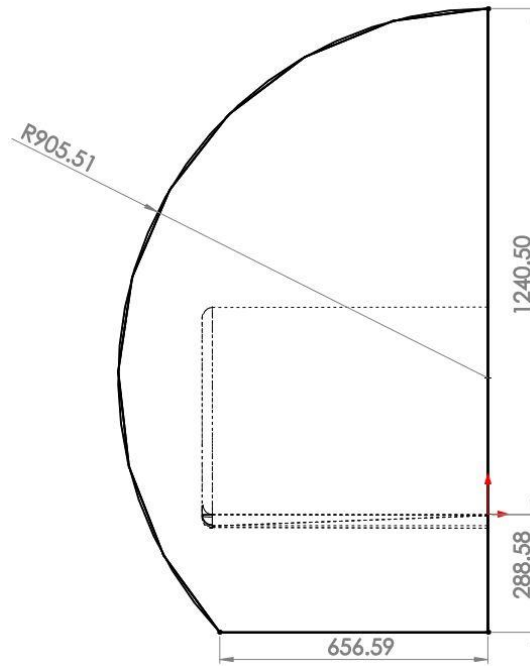


Figure 3.2. Front view of tube (dimensions in mm)

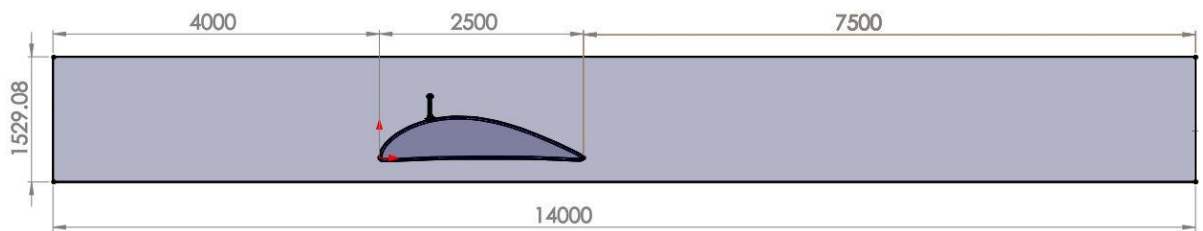


Figure 3.3. Geometry domain (tube and pod positions, dimensions in mm)

After the initial study for validation was completed, the pod geometry was altered in order to test the different brake geometry and orientations. The base design of the aerodynamic braking system had a flat brake plate of height 300 mm and length 501 mm, oriented at 90° from the surface of the pod, as shown in figures 3.4 and 3.5. The

pod with the brake plate at 90° has been considered case 0 or the baseline among all the test cases. The top and the bottom edges of the brake plate was filleted with a 20 mm radius and the front edge was filleted with a 10 mm radius. This is done in order to prevent any distortion that may occur during meshing and quantization. The flat brake plate was 30 mm thick and it was located 600 mm from the leading edge of the pod.

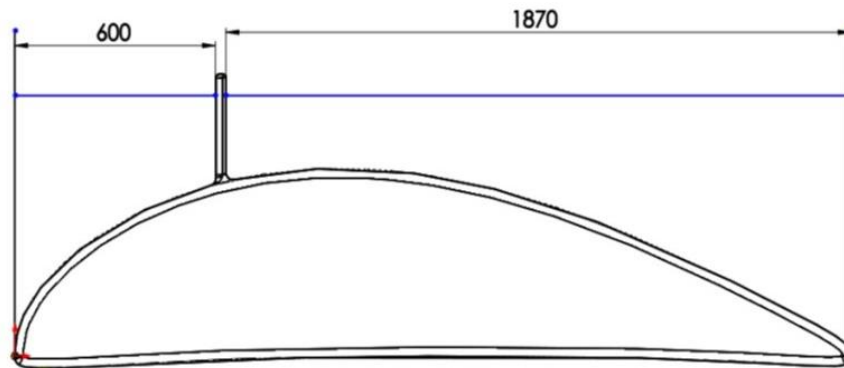


Figure 3.4. Position of brake relative to pod (dimensions in mm)

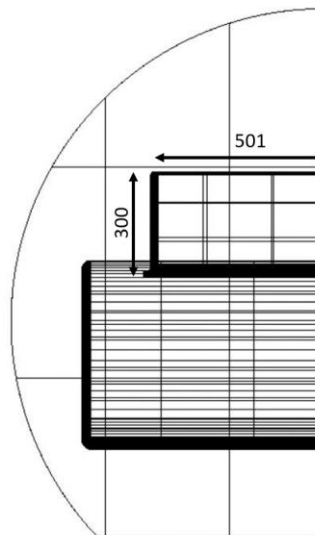


Figure 3.5. Front view of brake (dimensions in mm)

3.2 Variation of Brake Angle of Attack

The brake plate was designed to be perpendicular to the fluid flow, as this orientation provides maximum surface area and drag. The main design considerations which were

the focus of our study were the effect of brake plate orientation with respect to the axis of fluid flow on the drag and lift forces generated. After validation of the baseline flat brake plate at an angle of 90° was completed, there were two underlying features for the next phase of study. These were the effect of brake angle of attack on the fluid flow, and the effect of brake orientation, either facing toward, or away from the fluid, on the overall flow and circulation. The primary study was to place the flat brake plate at four distinct angles with respect to the plane of symmetry: 15° , 30° , 45° and 60° . It was noted that there were two distinct approaches to varying the angle of attack. One involved varying the brake plate while keeping the horizontal brake profile length of 501 mm constant; this was termed the constant profile approach. However, due to the limitations in the pod design, this approach does not allow brakes at 45° and 60° in the forward direction. The other approach, termed the constant length approach, had the brake plate length of 501 mm constant. In the former approach, the brake length changed to meet the desired angle, whereas in the second, the brake length remained same while the horizontal profile it created changed with change in orientation with respect to the plane of geometry.

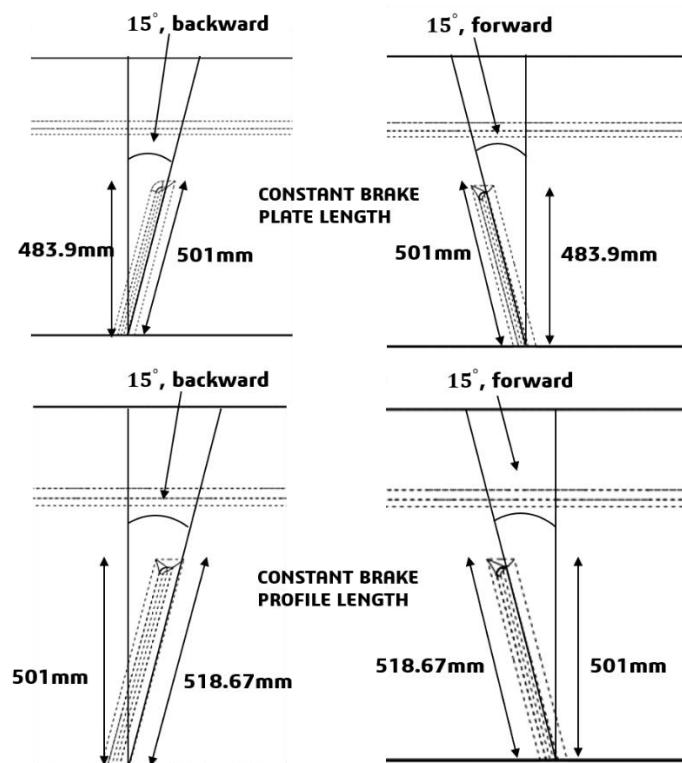


Figure 3.6. Brake approaches geometry (top view)

3.2.1 Constant Brake Plate Length

Table 3.1. Test cases of constant brake plate length

Case Number	Angle of attack (angle with axis of fluid flow)	Brake plate length	Brake profile length	Brake orientation
0 (baseline)	0	501	N/A	N/A
1	15	501	483.9	Backward
2	30	501	433.9	Backward
3	45	501	354.3	Backward
4	60	501	250.5	Backward
5	15	501	483.9	Forward
6	30	501	433.9	Forward
7	45	501	354.3	Forward
8	60	501	250.5	Forward

In this design approach (case 1 through 8), the length of the physical brake plate is kept constant at 501 mm, and it is oriented at 90° with respect to the pod. However, its angle of attack with respect to the axis of fluid flow is varied, and as a result, the effective brake profile of the plate is also varied. the angle of attack of the brake was varied to 15°, 30°, 45° and 60°, in both forward facing (cases 5 through 8) and backward facing (cases 1 through 4) arrangements. The plate is said to be forward facing if it moves toward the leading edge perpendicular to the axis of symmetry, and backward facing if it moves away from the leading edge perpendicular to the axis of symmetry.

3.2.2 Constant Brake Profile Length

Table 3.2. Test cases of constant brake profile length

Case Number	Angle of attack (angle with axis of fluid flow)	Brake plate length	Brake profile length	Brake orientation
0 (baseline)	0	501	N/A	N/A
9	15	518.67	501	Backward
10	30	578.5	501	Backward
11	45	708.52	501	Backward
12	60	1002	501	Backward
13	15	518.67	501	Forward
14	30	578.5	501	Forward

In this design approach (case 9 through 14), the length of the physical brake plate is varied. It is oriented at 90° with respect to the pod, with varying angle of attack with respect to the axis of fluid flow. However, as the effective brake profile of the plate is kept constant at 501 mm, the brake plate length varies with variation in attack angle. As before, the angle of attack of the brake was varied to 15°, 30°, 45° and 60°, in both forward facing (cases 13 and 14) and backward facing (cases 9 through 12) arrangements. However, due to the limitations in the pod design, this approach does not allow brakes at 45° and 60° in the forward direction.

3.3 Multiple or Split Brakes

The second design aspect to be studied was the use of multiple flat brake plates at an angle of 90° spread out over three positions of the pod, effectively splitting a single brake and positioning it at different points along the pod length. The effective profile length of the configuration of plates in all cases was kept at 501mm. The brake plate was oriented at 90° in the base design as it produced the greatest amount of drag force.

The pod with the single brake plate had the plate positioned at 0.24 of the pod chord length.

The first model (case 15) had the 501 mm brake plate divided into three equal lengths. The first 167 mm plate started from the symmetrical plane and was positioned at 0.24 of the chord length. The second 167 mm plate started from 167 mm away from the symmetrical plane while being positioned at 0.5 of the chord length. The third and final 167 mm plate was positioned at 0.75 of the chord length and started from 334 mm away from the symmetrical plane. The aim of this configuration was to avoid a subsequent brake plate falling inside the wake region of its previous plate. As such, the plates were moved further away from the plane of symmetry as they moved further along the chord length of the pod.

The second model (case 16) used two flat brake plates. The first plate was at 0.24 of the chord length and was 167 mm in length. The second plate was 501 mm long, started from the symmetrical plane and was located at 0.75 of the chord length. This second plate thus acted the same as the original single brake plate configuration but placed further along the chord length.

The third model (case 17) studied had a 501 mm brake plate at the 0.24 chord length, with another plate of the same dimensions located at 0.0306 of the chord length, which is a point immediately downstream of the leading edge of the pod. This model was designed to study the effects of a secondary plate located near the point of maximum pressure or the leading edge, on subsequent fluid flow and fluid vorticity.

Table 3.3. Test cases for multiple or split brakes configuration

Case No.	Number of plates used	Brake1			Brake 2			Brake 3		
		Location along pod chord	Length of plate	Distance from axis of symmetry	Location along pod chord	Length of plate	Distance from axis of symmetry	Location along pod chord	Length of plate	Distance from axis of symmetry
15	3	0.24	167	0	0.5	167	167	0.75	167	334
16	2	0.24	167	0	0.75	501	0	-	-	-
17	2	0.0306	501	0	0.24	501	0	-	-	-

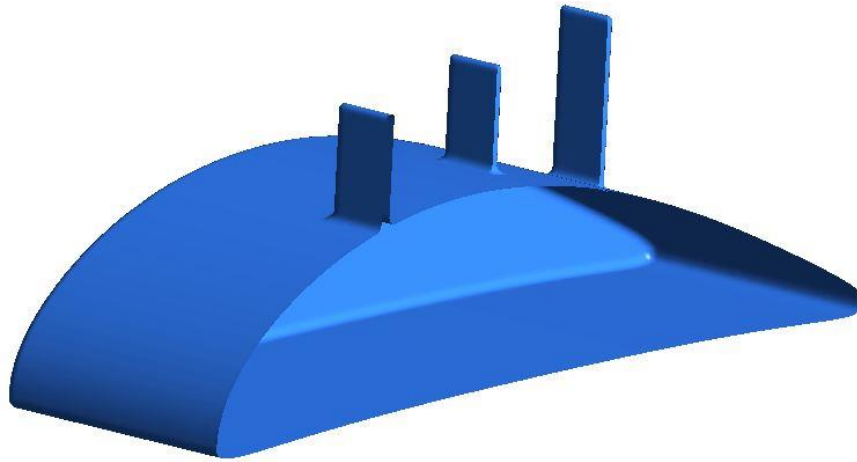


Figure 3.7. Case 15 (3 brakes of equal length)

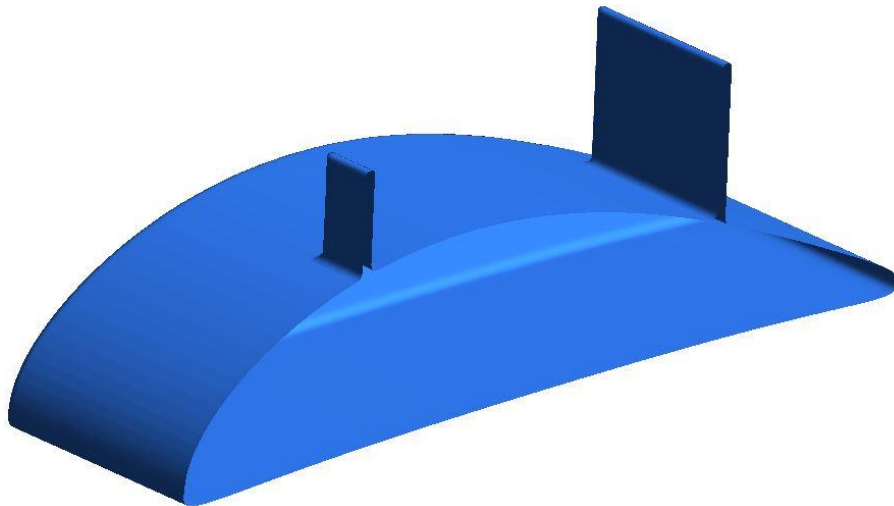


Figure 3.8. Case 16 (2 brakes of different length)

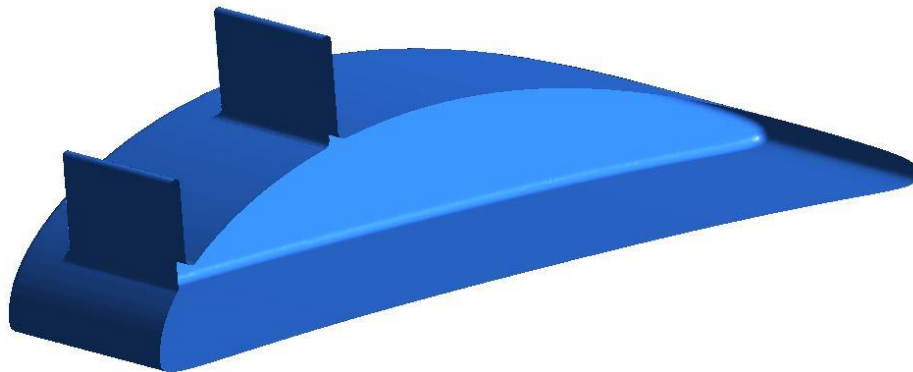


Figure 3.9. Case 17 (2 brakes of equal length)

3.4 Computational Grid and Quantization

The focus of this study was the brake force generated on the different cases of brake plate arrangement, the pressure differential created on either side of the brake plate, the presence of phenomena such as vorticity and wake regions that may affect the fluid flow.

The domain defined for study is a scaled down model of the practical case. The dimensions have been scaled down in order to reduce computational power, and to provide more dense mesh arrangement and thus produce more accurate results.

For analyzing the drag and flow characteristics, geometries were generated for each of the angled and split brake cases as well as for the slotted brake cases. These geometries were then imported into ANSYS ICEM and meshed. The meshing parameters are detailed below. ANSYS ICEM was used in this application due to its robust nature and reliability when dealing with complex geometry.

3.5 Mesh Quality and Grid Independence

For accurate solutions to be produced, the numerical solution of the differential equations must achieve proper convergence. For this to occur, the computational grid, i.e. mesh, must be of proper quality, as low-quality mesh may result in distortion of the geometry and computational grid, producing inaccurate results. A sample mesh is shown in figure 3.10.



Figure 3.10. Grid resolution across domain

The main points of interest in this study is the flow at the leading edge, as well the flow surrounding the brake plates and also the wake region. The close region around the pod and brake was of high interest as this was the region of boundary layer separation, pressure gradients and wake formation. As such, high density mesh has been used in this region in order to obtain accurate values for flow parameters. The

INLET, OUTLET, WALL and SYMMETRY sections have relatively coarser meshing, and this allows the simulation to require less computational power during solution procedure.

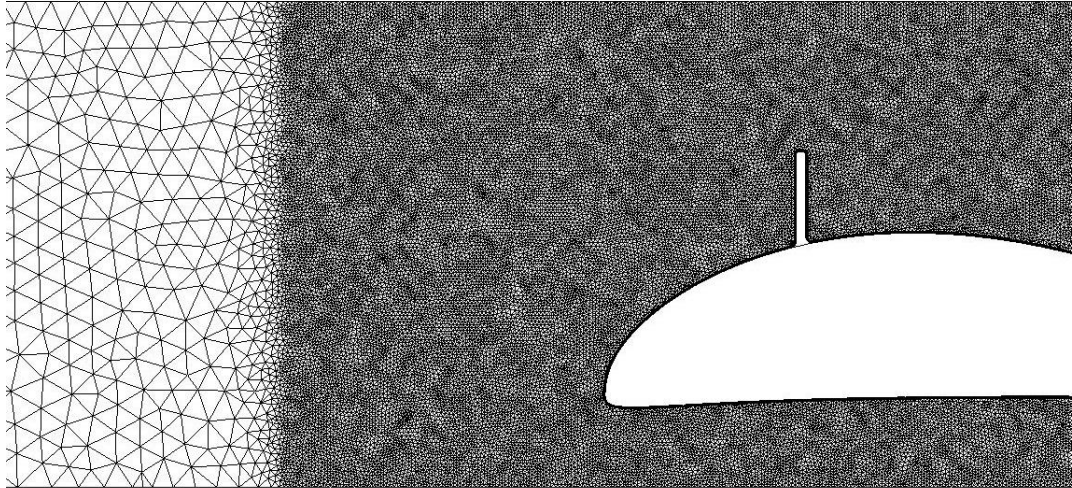


Figure 3.11. Grid resolution across specific domain

Global mesh size was set at 80 while the section around the pod and brake surface had a denser mesh of size 20, with a prism of 15 layers and expansion factor of 1.4, with a first cell thickness of 0.00002 mm being used in order to provide better accuracy for the immediately surrounding flow regime.

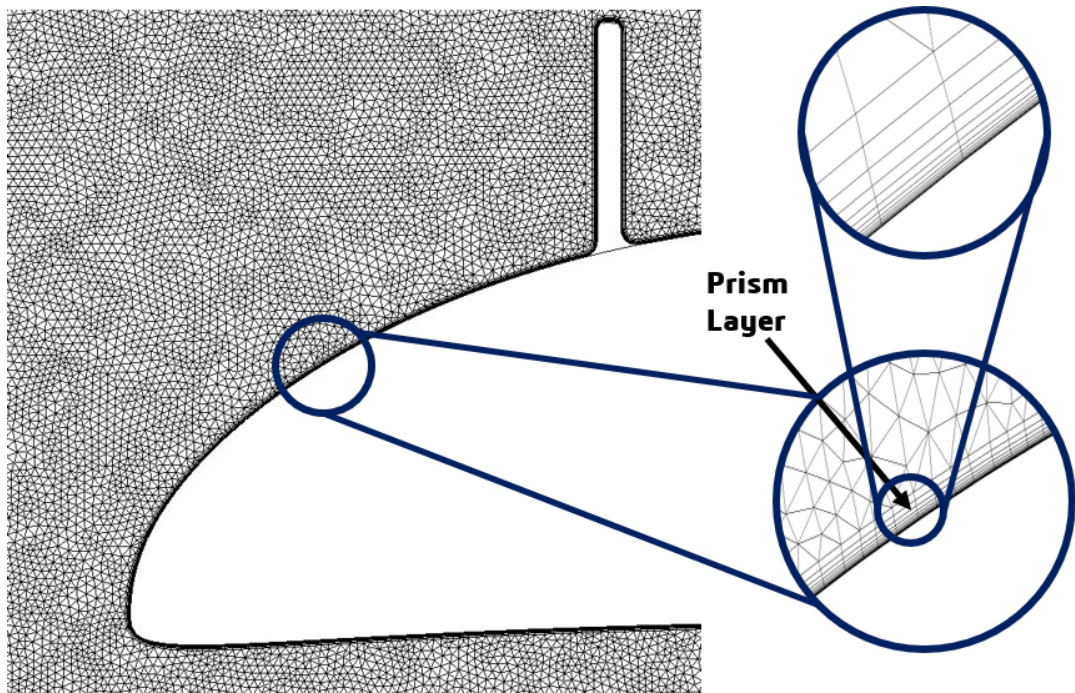


Figure 3.12. Enlarged view of prism layers in region of finer mesh

Due to the nature of the fluid flow, $k-\omega$ SST was employed as the turbulence model because of its commendable attitude in adverse pressure gradients and good near wall performance. The SST model suitably changes to $k-\varepsilon$ model in the free-stream while functioning well in the area close to the tube walls [16]. In accordance with the prerequisite of the SST model, the average $Y+$ value was below 1; 0.55 for the pod and 0.43 for the brake. A steady state analysis was carried out with the convergence criteria set at $1e-4$. Oscillations of residuals generally reduced after 50 iterations.

The first cell thickness is related to the $Y+$ value by the equation [29],

$$\Delta y_1 = \frac{y + \mu}{\rho \cdot U_\tau} \quad (3.1)$$

The frictional velocity U_τ is given by the equation;

$$U_\tau = \sqrt{\frac{\tau_w}{\rho}} \quad (3.2)$$

where, wall shear stress τ_w can be found by the relation

$$\tau_w = \frac{1}{2} C_f \rho U^2 \quad (3.3)$$

There is, however, implicit uncertainty in the value of $Y+$ due to the value of C_f used being an estimation, obtained from the empirical relation for external flow over simple geometry;

$$C_f = 0.058 Re^{-0.2} \quad (3.4)$$

Due to complex geometry, unstructured meshing was used in order to more accurately capture the computational domain, with the mesh grid having a least quality of 2.5 while the overall mesh grid quality was skewed towards 0.7-0.8. The mesh quality is detailed in figure 3.13.

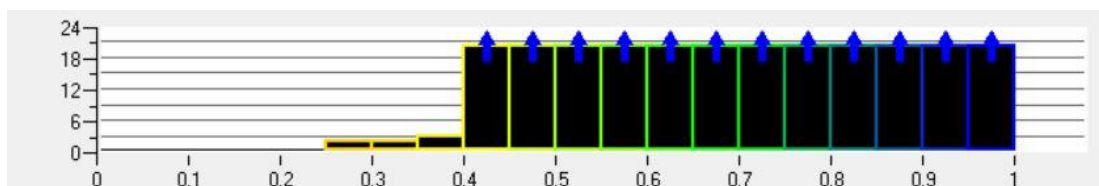


Figure 3.13. Overall mesh grid quality

The grid sensitivity test has been carried out with respect to both the average Mach number and the average pressure over the plane of symmetry. As seen from figure 3.14, in both cases, a significant increase is observed with the initial increase in node count from 1.8 million to 2.3 million. The change of values is 16% for the average Mach number and 0.17% for the average pressure. However, with subsequent increase in node count from 2.3 million to 2.9 million, the changes in Mach number and pressure are negligible, the change in Mach number being 0.59% and the change in pressure being 0.026%. These results allowed for the interpretation that grid independence has been achieved and hence, the node count has been kept at 2.3 million.

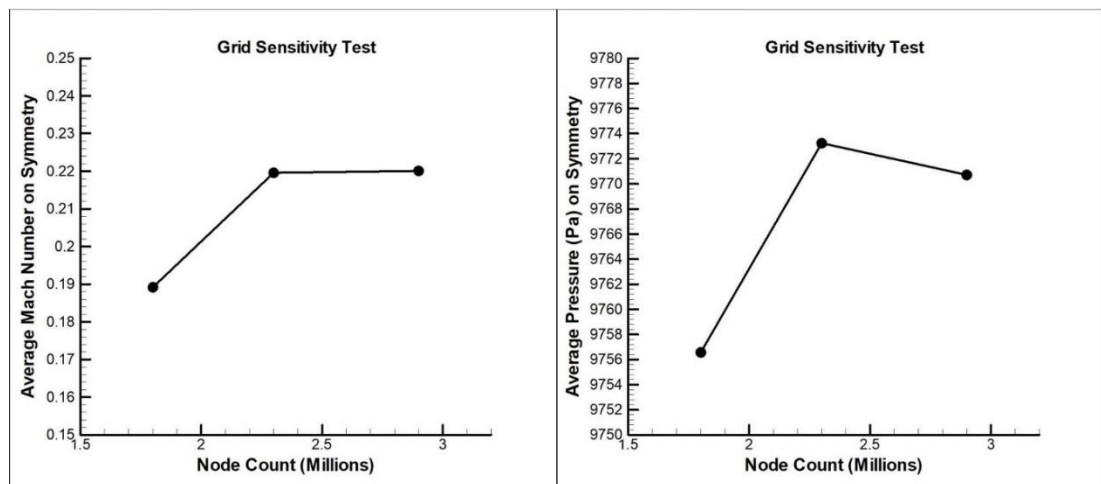


Figure: 3.14. Grid sensitivity test

3.6 Boundary Conditions

On the test domain, total pressure imposed at the INLET was 11 kPa and the OUTLET static pressure was 10 kPa. Total temperature was taken to be 336 K. The pod walls are classified as no slip walls in order to account for viscous effects and thus more accurately capture the fluid flow, while the tube walls are modeled as free slip walls as there is no relative motion between the tube walls and the fluid. The xy-plane of the geometry, which is also the plane of symmetry of the pod, is classified as SYMMETRY. Steady-state analysis was carried out on half of the geometry, across the symmetry plane, in order to lower the computational power required.

The inlet pressure was considered around 100 Pa by Musk [1] in the initial white paper, however as concluded by both Braun et al [2] and Chen et al [5], the reduction of pressure from 10 kPa to 100 Pa does not result in significant reduction in drag, and as such the reduction in drag is not economically feasible when compared to the energy and cost required to maintain the low pressure. While the work of Chen et al [5] was regarding Evacuated MAGLEV Trains, the work has enough similarities with the Hyperloop for the findings to be appropriate.

The boundary conditions are thus summarized as below –

TOTAL PRESSURE	11 kPa
TOTAL TEMPERATURE	336 K
OUTLET STATIC PRESSURE	10 kPa
POD AND BRAKE WALL CONDITION	NO SLIP WALL
TUBE WALL CONDITION	FREE SLIP WALL
TURBULENCE MODEL	$k - \omega$ SST MODEL

3.7 Validation

For validation, the results have been compared with isentropic flow conditions for the reduced model. Figure 3.14 shows the Mach number distribution over the length of the pod obtained from simulation results and from isentropic conditions. The isentropic plot is generated using equation 2.4, and the simulation plot is obtained from CFD-Post, after running a simulation on a no-brake geometry. These two plots have been combined together in figure 3.14. The drag value was found to be around 170 N in the no-brake geometry which is within 5% of the drag value obtained by Braun et al. [2] in their maximum lift (extruded) design. The isentropic plot is found by calculating the average Mach values using equation 2.4 for the entire flow region excluding the pod at different planes along the direction of fluid flow. Similarly, the 3D simulation values were calculated using the same approach with the values being calculated using CFD-Post. The plots obtained are shown in figure 3.14 and it is observed that the two graphs approximate each other with the difference in values occurring due to the isentropic condition.

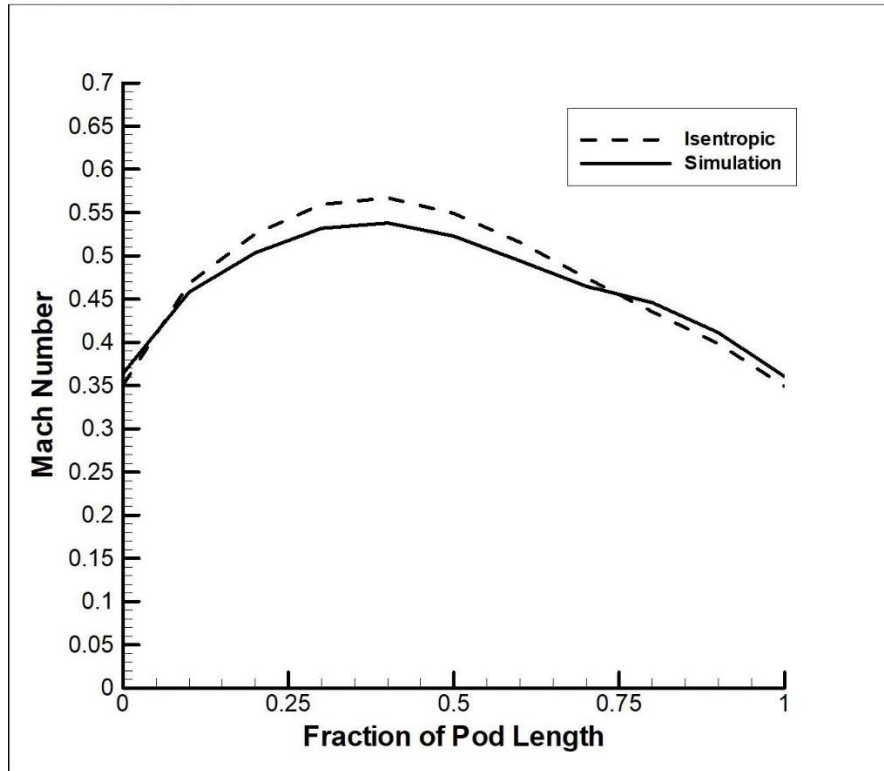


Figure 3.14. Mach number across pod length obtained from reduced model and simulation results

Chapter 4

Results for Angled Brakes

The convergence criteria for all of mass, momentum and energy was set to 10^{-4} and it was found that after around 85 iterations the residuals stabilized at about 73 m/s velocity and no significant change in this magnitude of velocity occurred over time. To generate the graph, a user point was created during setup in Ansys CFX to observe the velocity.

It was decided that a solution of this precision will be sufficient for this study because a solution of higher accuracy does not outweigh the benefit of obtaining them at a cost of higher computational time and power. Nevertheless, 150 iterations were used for solution in the study with enough justification and proper precaution taken to observe the residuals during solution.

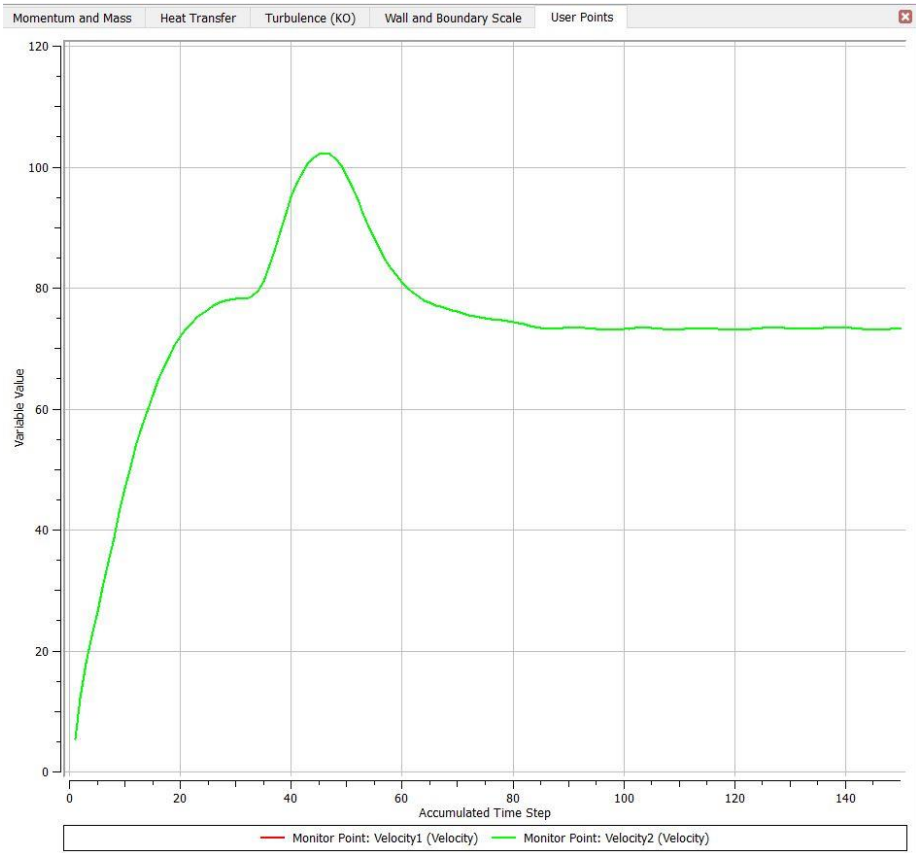


Figure 4.1. Variation of residuals at a given point

The drag forces on the pod and the brake were individually observed and summed up to find the total drag force. These forces are tabulated in the following table. Variation of the total drag force was found by plotting the total drag force against the different blade angles.

Table 4.1. Test cases for constant brake length and their resulting drag forces

Approach	Constant Brake Length							
Orientation	Backward				Forward			
Angle	15°	30°	45°	60°	15°	30°	45°	60°
Drag (N)	689.6	662.3	596.1	507.3	663.4	601.7	483.2	381.5

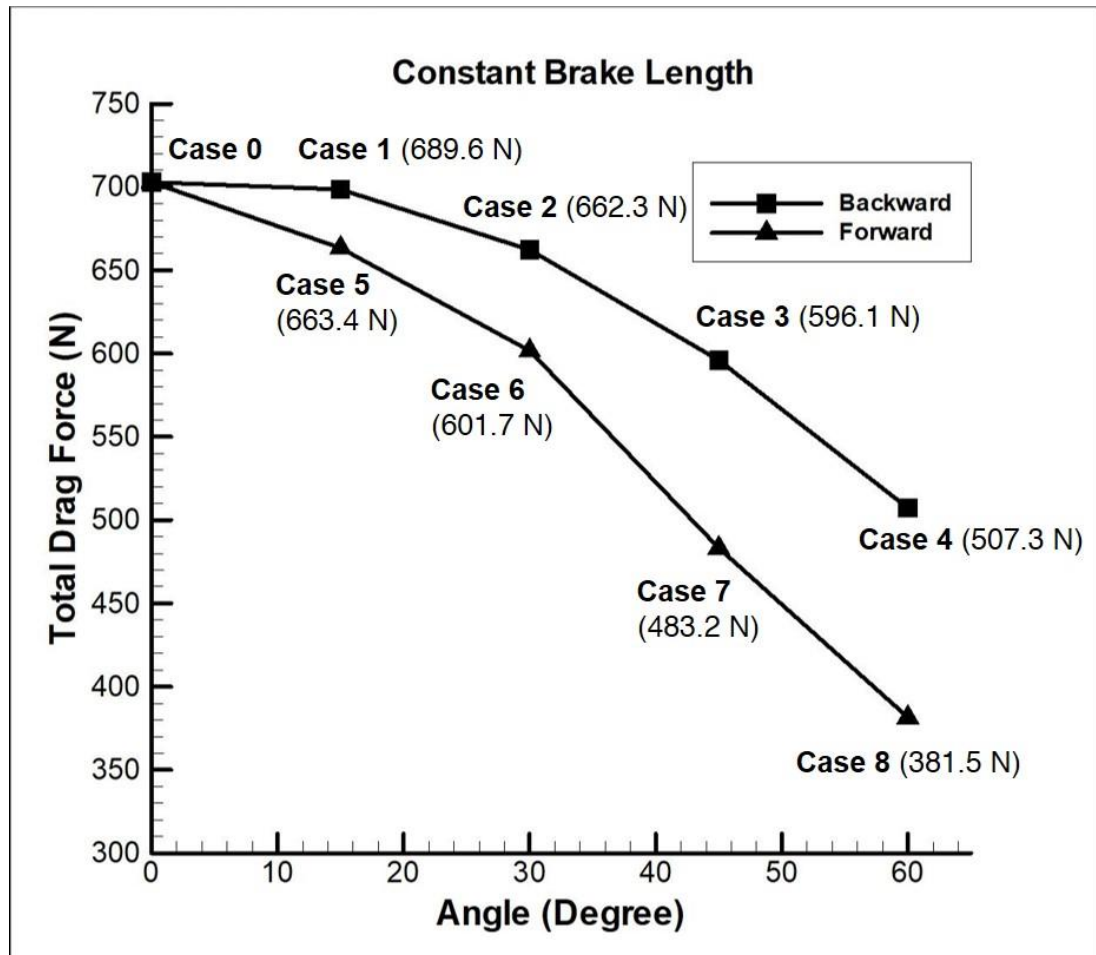


Figure 4.2. Variation of drag force for constant brake length

Table 4.2. Test cases for constant brake profile and their resulting drag forces

Approach	Constant Brake Profile					
Orientation	Backward				Forward	
Angle	15°	30°	45°	60°	15°	30°
Drag (N)	710.8	689.5	637.6	571	666.4	640.1

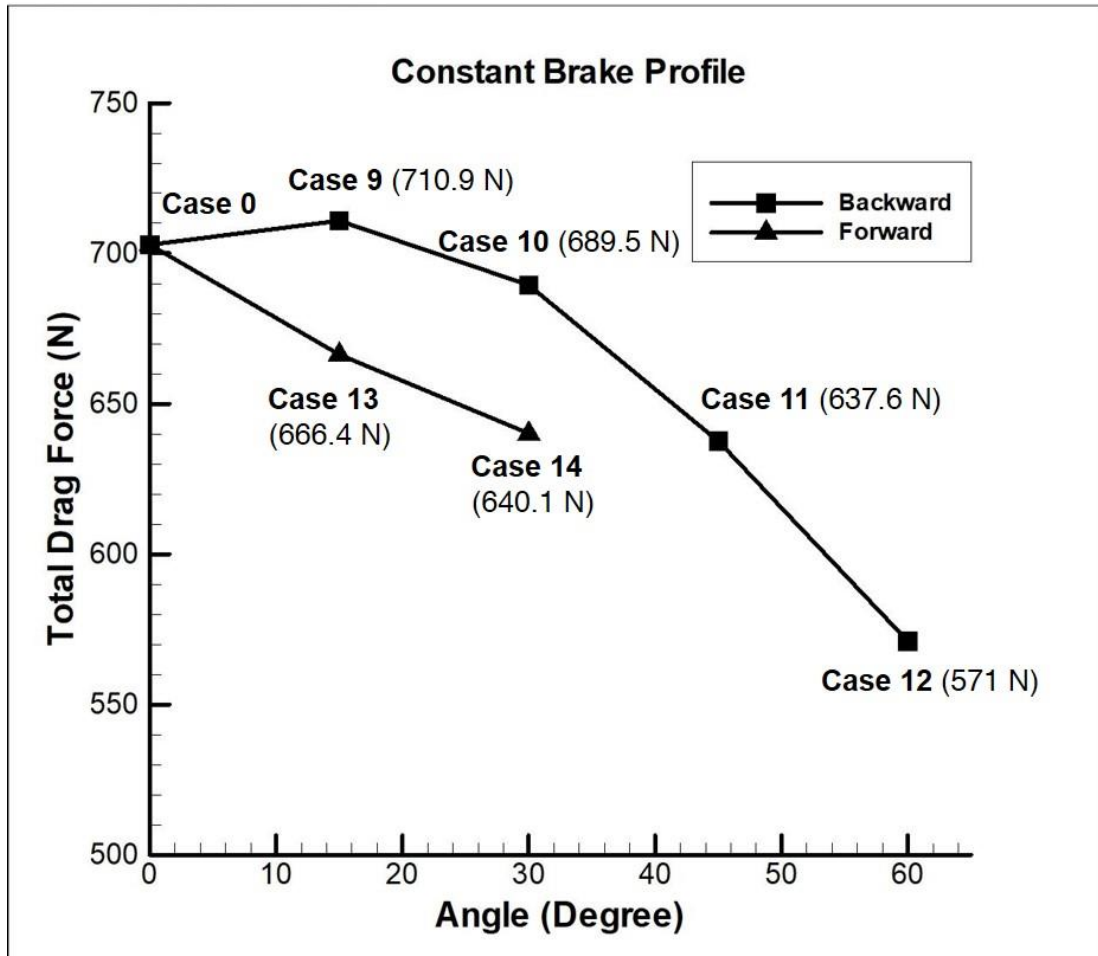


Figure 4.3. Variation of drag force for constant brake profile

As seen from the plots, the total force decreases as the angle of the brake plate increases, both in the forward and backward directions. The highest force observed is at 15° backward for the case of constant brake profile (case 9). It is also seen that for both the constant brake length and the constant brake profile, the backward-angled brake geometries produce higher drag forces than the forward-angled ones.

Since the 15° backward-angled constant brake profile case produced the highest drag, further simulations were carried out focusing on that region to see whether the maximum drag occurred elsewhere in the 10°-20° region. The total drag found at 10°, 14°, 15°, 16° and 20° were observed and plotted.

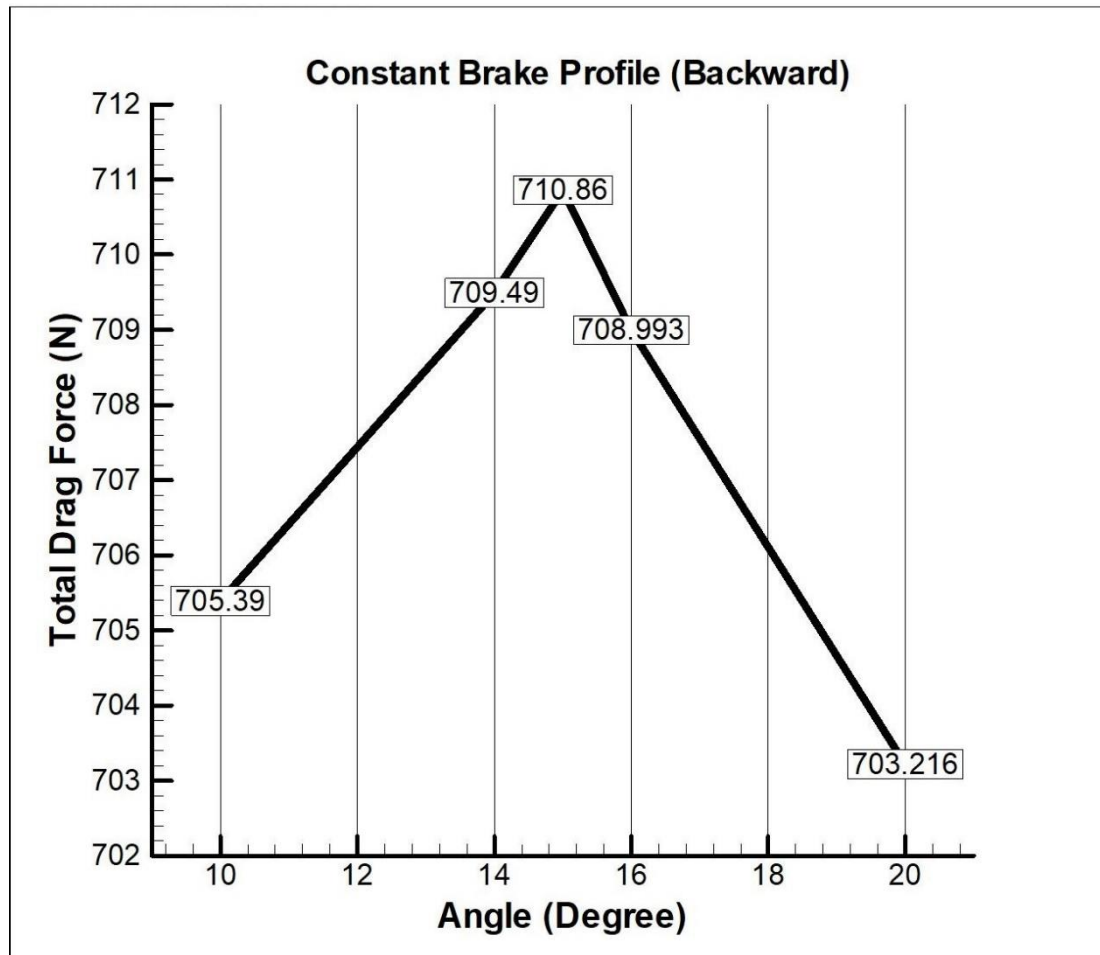


Figure 4.4. Variation of drag force in the 10°-20° region for constant brake profile

The 15° brake still remained the highest drag producer. Initially it seemed that the baseline geometry (case 0) would produce the highest drag since the majority of the drag is due to pressure drag. Angling the brake would result in a decrease of the normal force exerted on the plate, leading to a decrease in drag. But angling the brake while keeping the profile constant results in an increased brake area. The result of this increased brake area outweighs the loss of normal force and hence the total drag increases up to 15°. After 15°, the advantage of increased brake area gets outweighed by the loss of normal force, and hence, the total drag decreases. So, 15° can be

considered as the optimum brake angle for the Hyperloop pod. Apart from the total drag force, Mach number and pressure contours have been drawn for all 14 cases and are presented below –

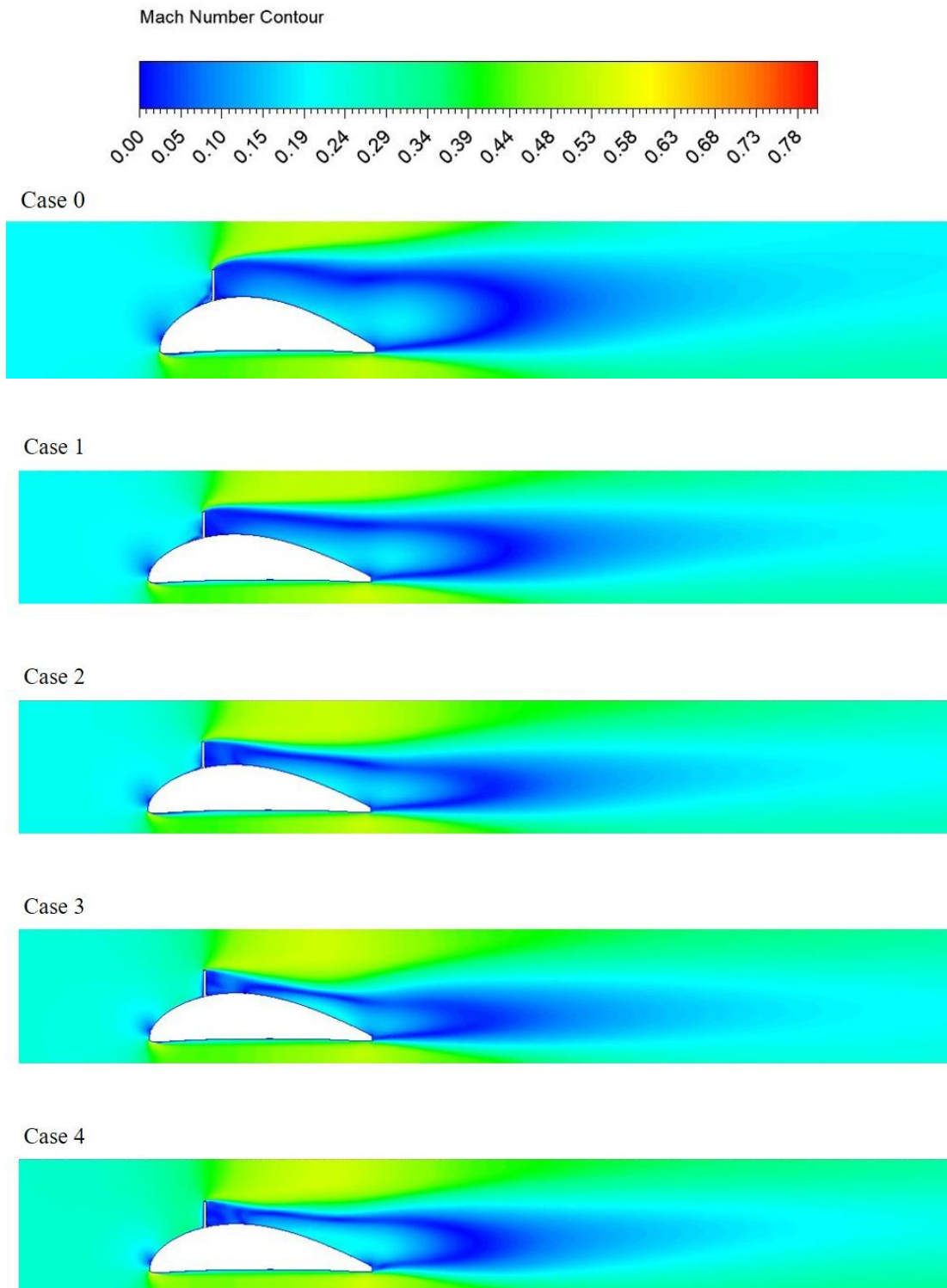


Figure 4.5. Mach number contours of cases 0-4

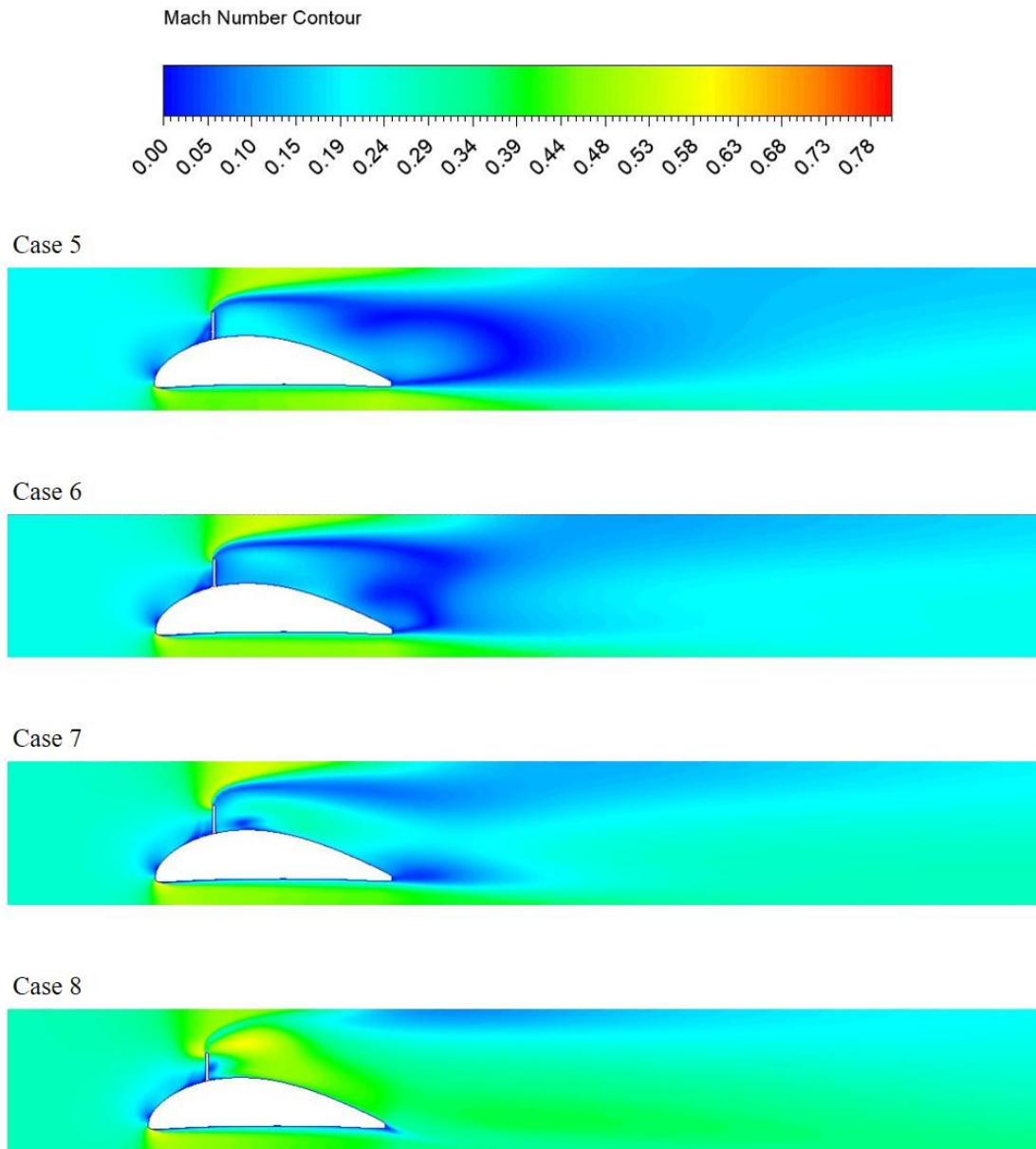
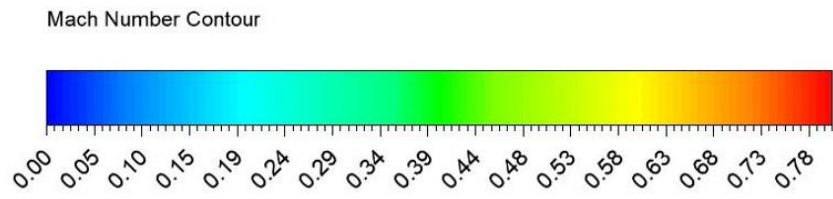
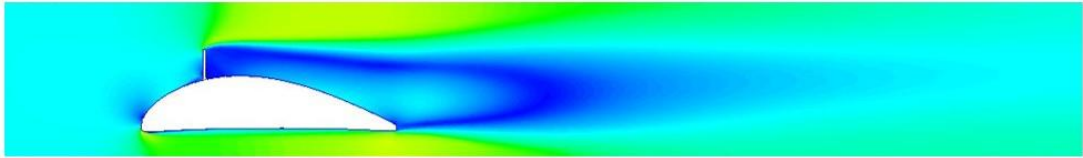


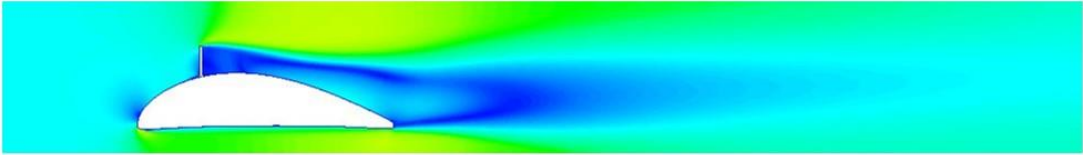
Figure 4.6. Mach number contours of cases 5-8



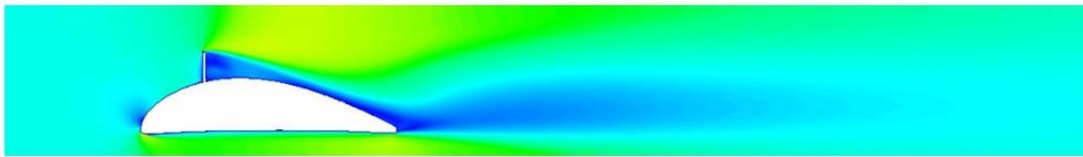
Case 9



Case 10



Case 11



Case 12

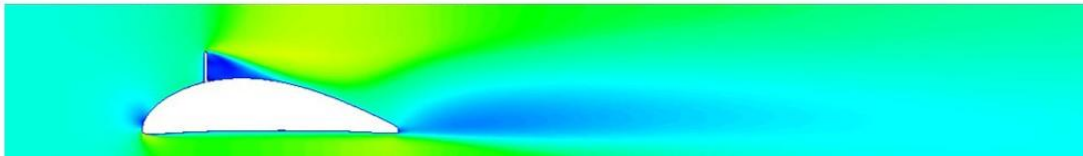
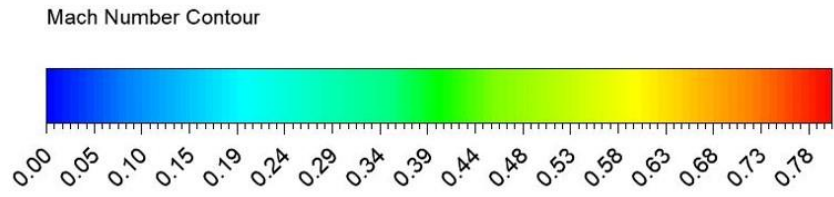
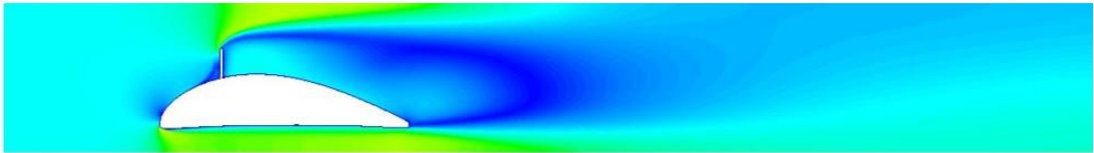


Figure 4.7. Mach number contours of cases 9-12



Case 13



Case 14

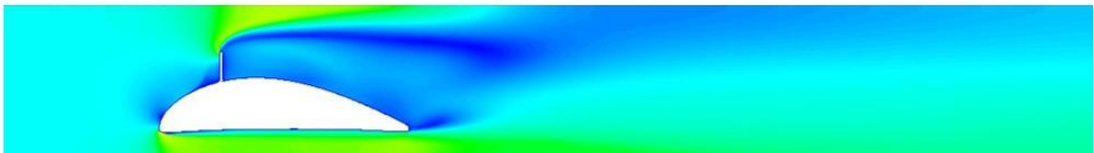


Figure 4.8. Mach number contours of cases 13-14

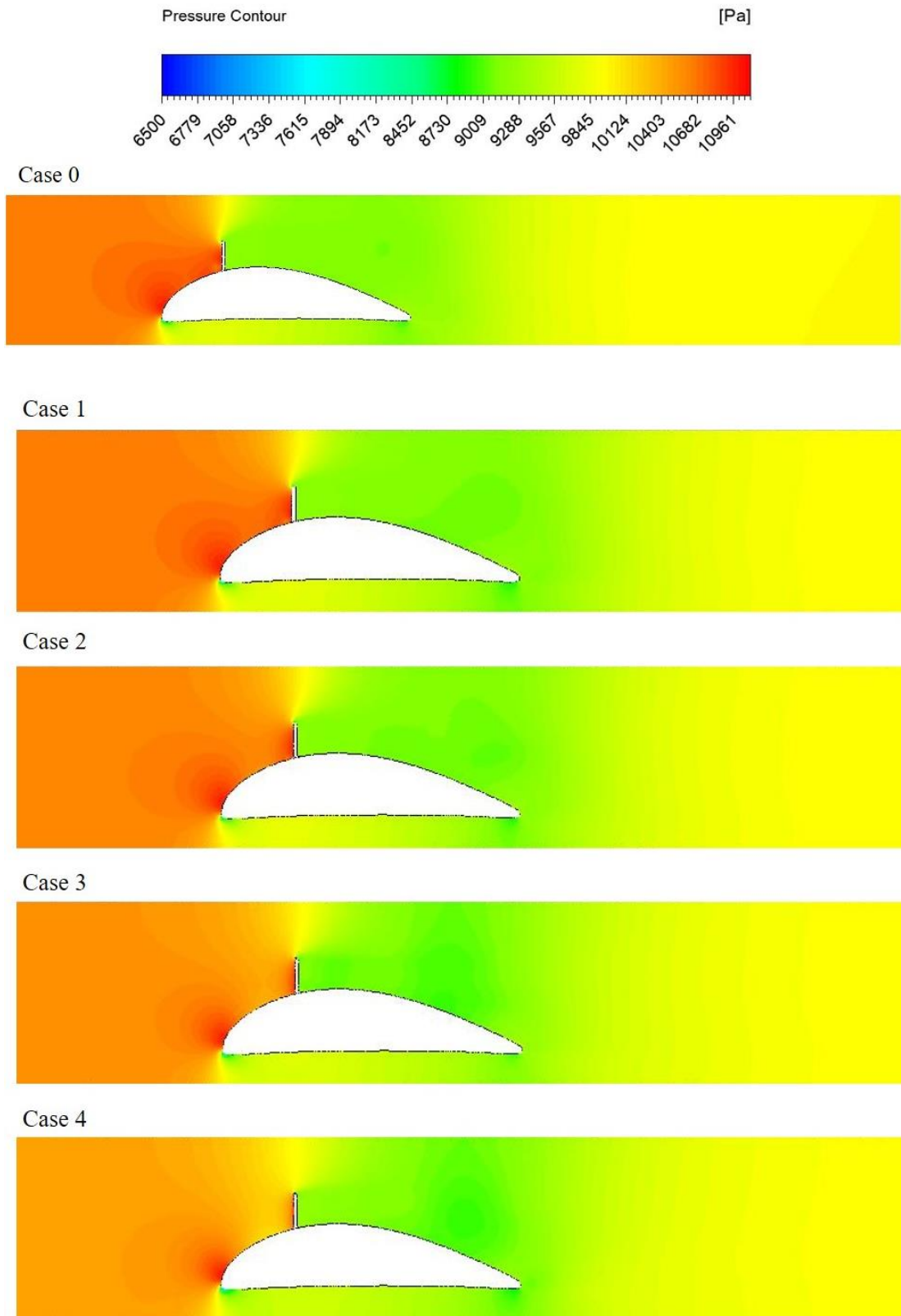


Figure 4.9. Pressure contours of cases 0-4

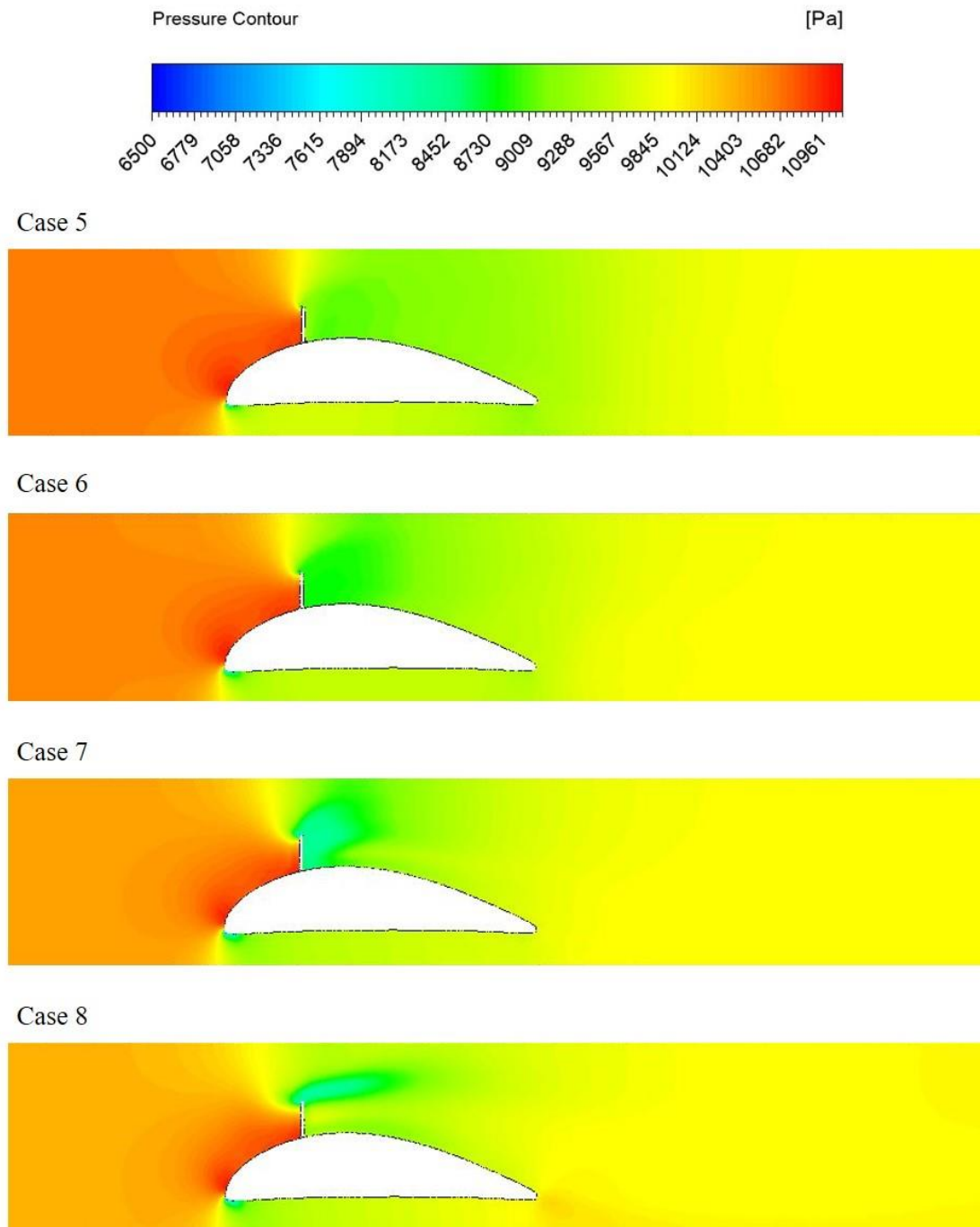


Figure 4.10. Pressure contours of cases 5-8

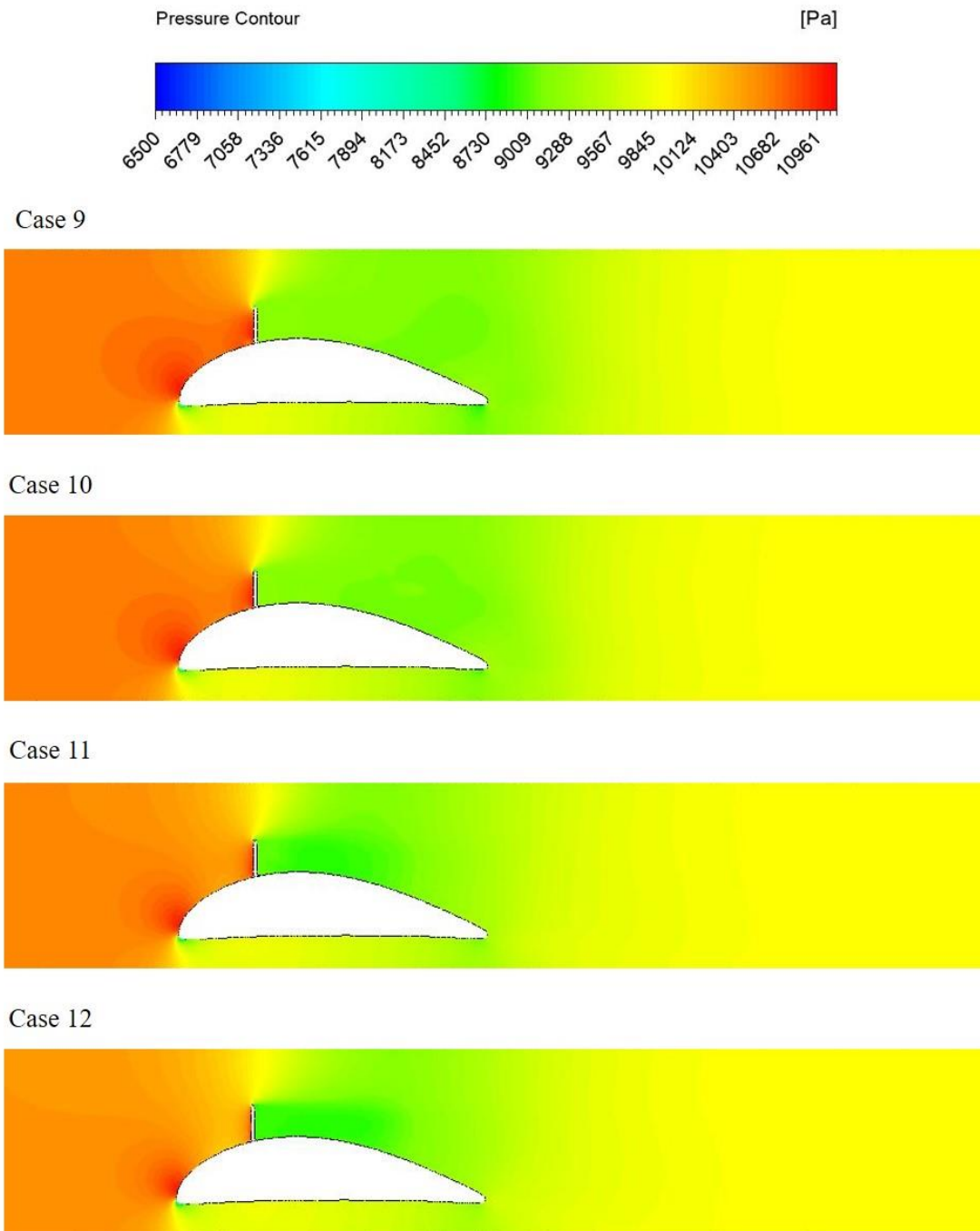
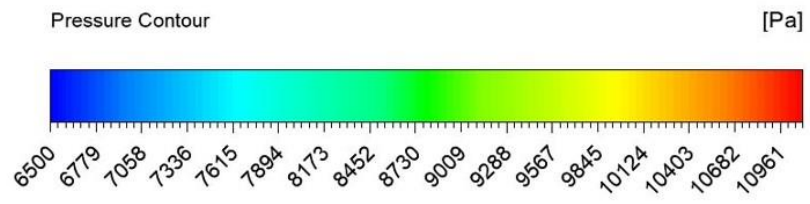
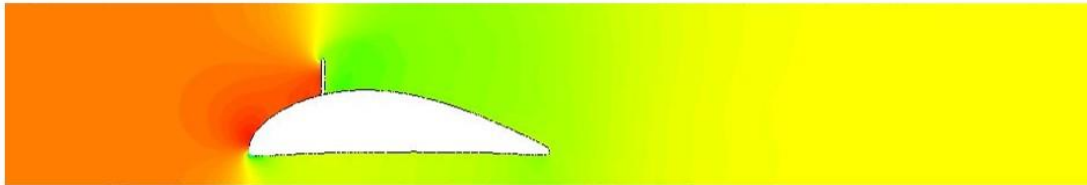


Figure 4.11. Pressure contours of cases 9-12



Case 13



Case 14

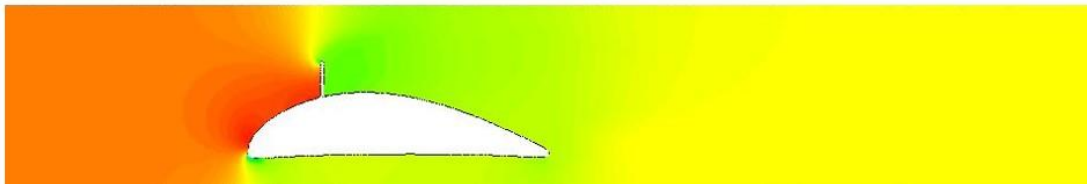


Figure 4.12. Pressure contours of cases 13-14

To gather a more in-depth idea about the flow behavior in some desired regions, 4 lines were drawn at locations illustrated below, and the Mach number and pressure distribution on these lines were plotted.

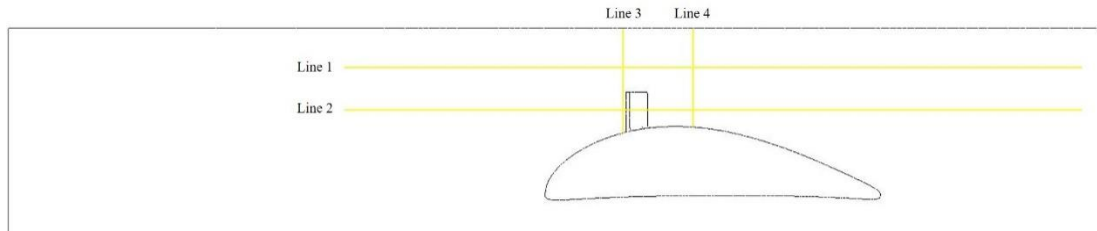


Figure 4.13. Nomenclature of the lines

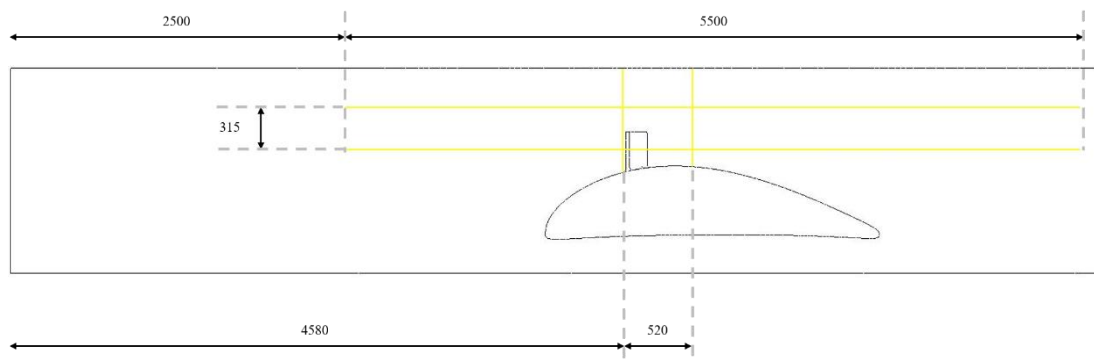


Figure 4.14. Specifications of the lines (dimensions in mm)

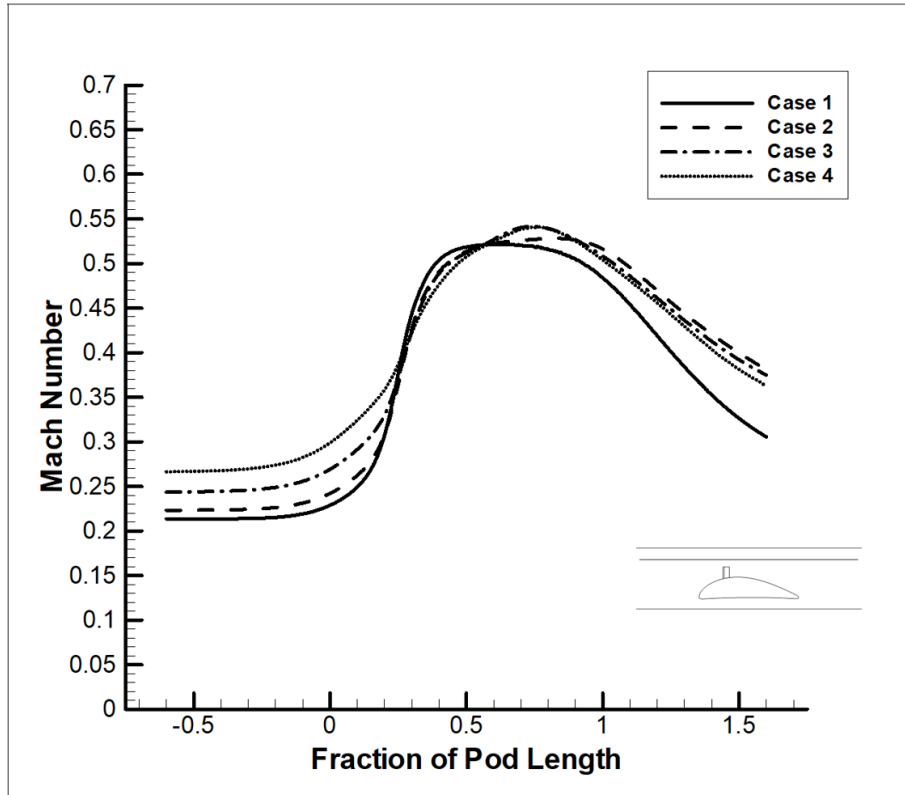


Figure 4.15. Mach number distribution along line 1 for cases 1-4

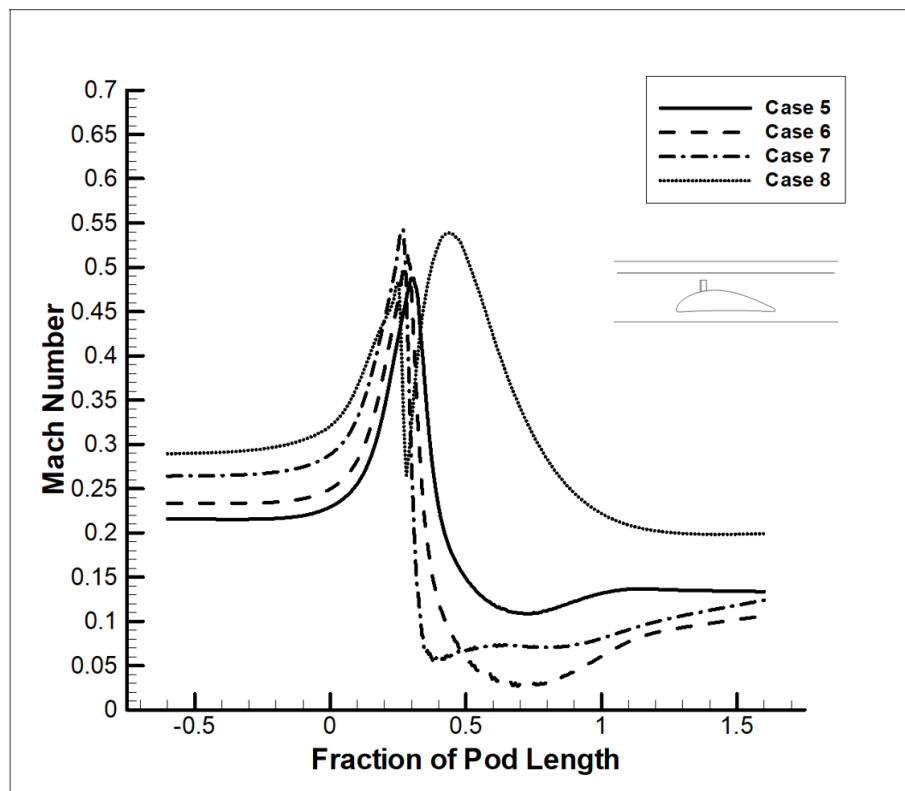


Figure 4.16. Mach number distribution along line 1 for cases 5-8

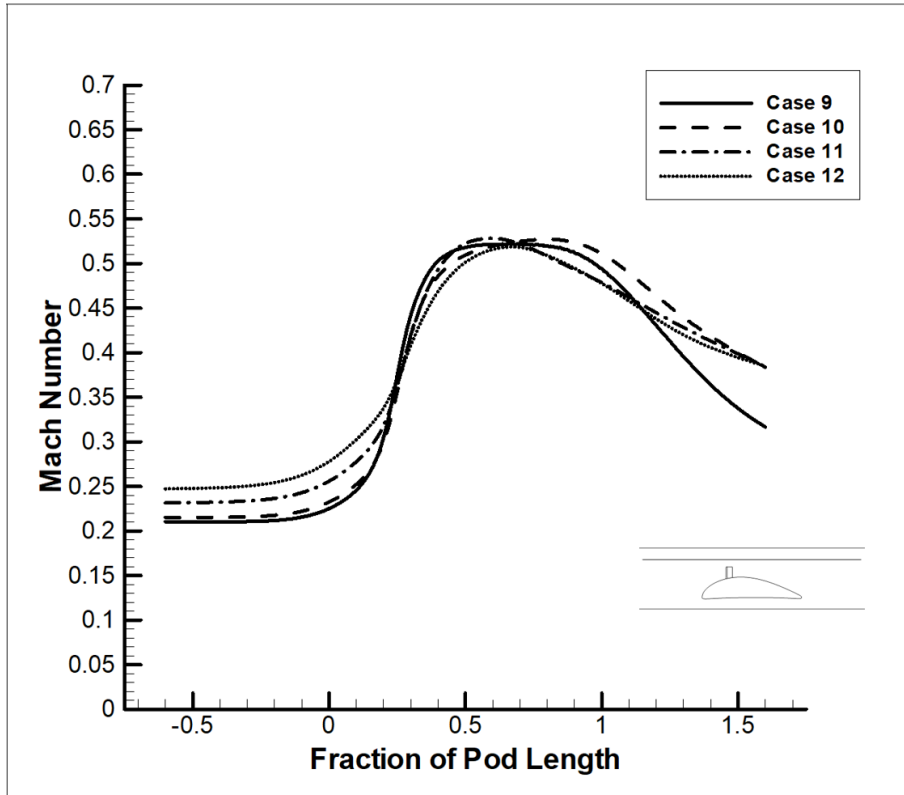


Figure 4.17. Mach number distribution along line 1 for cases 9-12

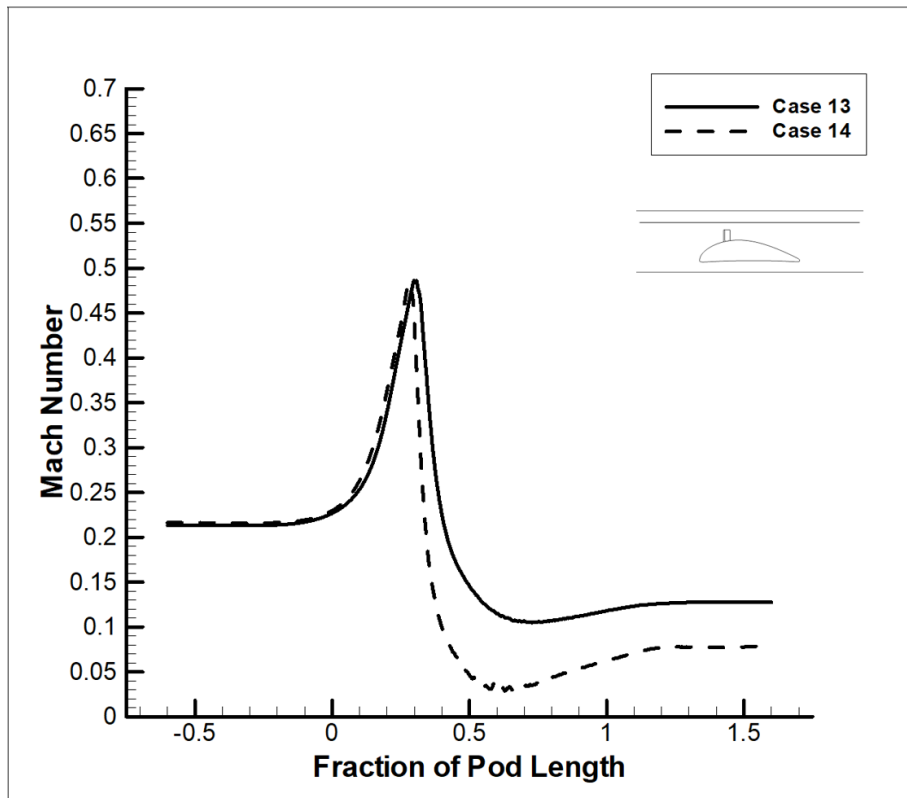


Figure 4.18. Mach number distribution along line 1 for cases 13-14

In all cases, there is a sharp rise in Mach nearer to the pod, as the fluid around it is displaced and accelerated upwards. For both constant brake plate and constant brake profile approach, it is observed that the Mach number rises with increase in attack angle, i.e. fluid accelerates with increase in attack angle. The peak Mach number occurs immediately above the pod in almost all cases, with it subsequently falling as flow moves away from and beyond the pod. In backward facing brakes the fall is more gradual, whereas it is more rapid and fluctuating for forward facing cases. Slightly higher peak Mach values are seen in constant profile cases compared to constant brake length cases. Overall, all peak values are in the range of 0.45 Ma to 0.53 Ma. The peaks occur earlier for forward facing cases, at or before 0.24 chord, i.e. from the chord length that the brake plate encounters the flow, whereas for backward facing plate peak occurs at 0.5 chord or beyond, as the brake plate interacts with the fluid further along the pod length.

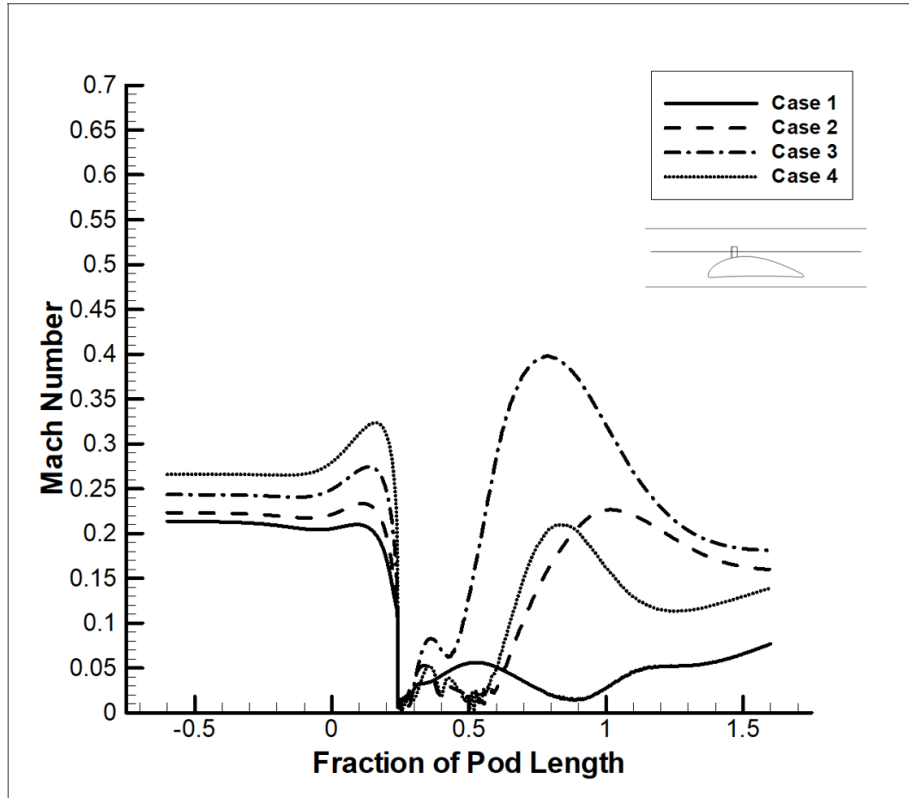


Figure 4.19. Mach number distribution along line 2 for cases 1-4

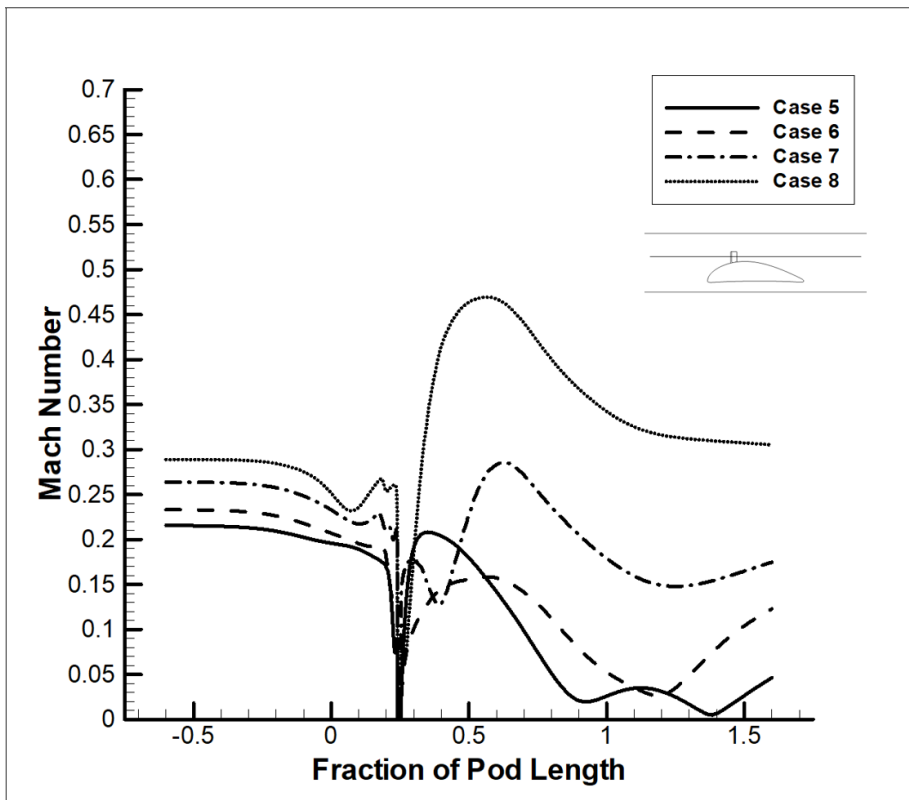


Figure 4.20. Mach number distribution along line 2 for cases 5-8

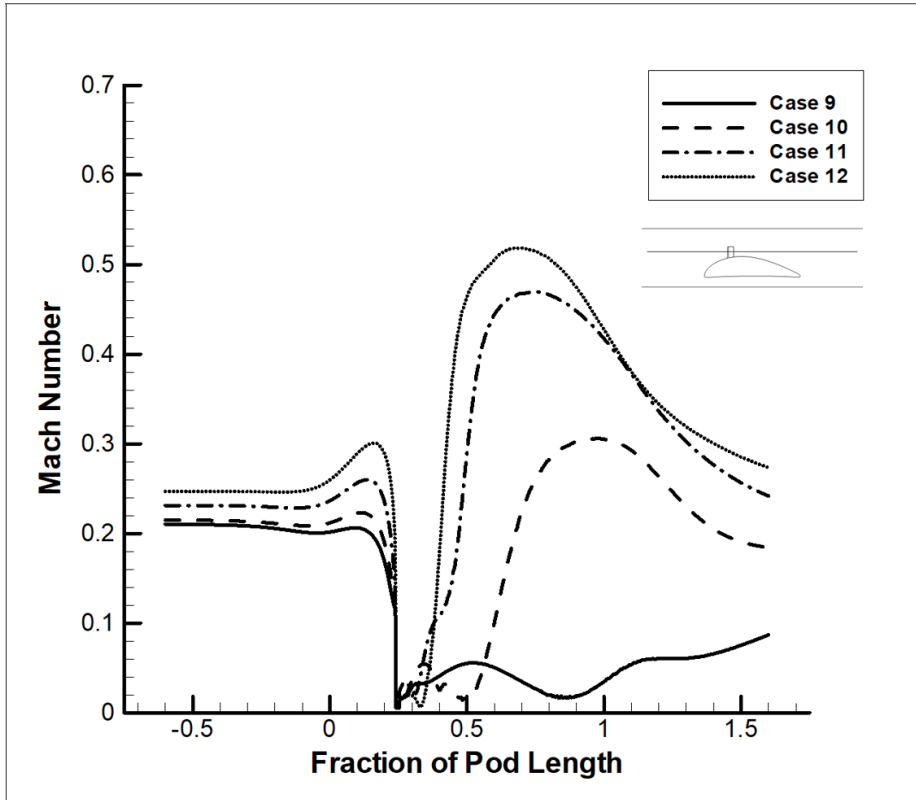


Figure 4.21. Mach number distribution along line 2 for cases 9-12

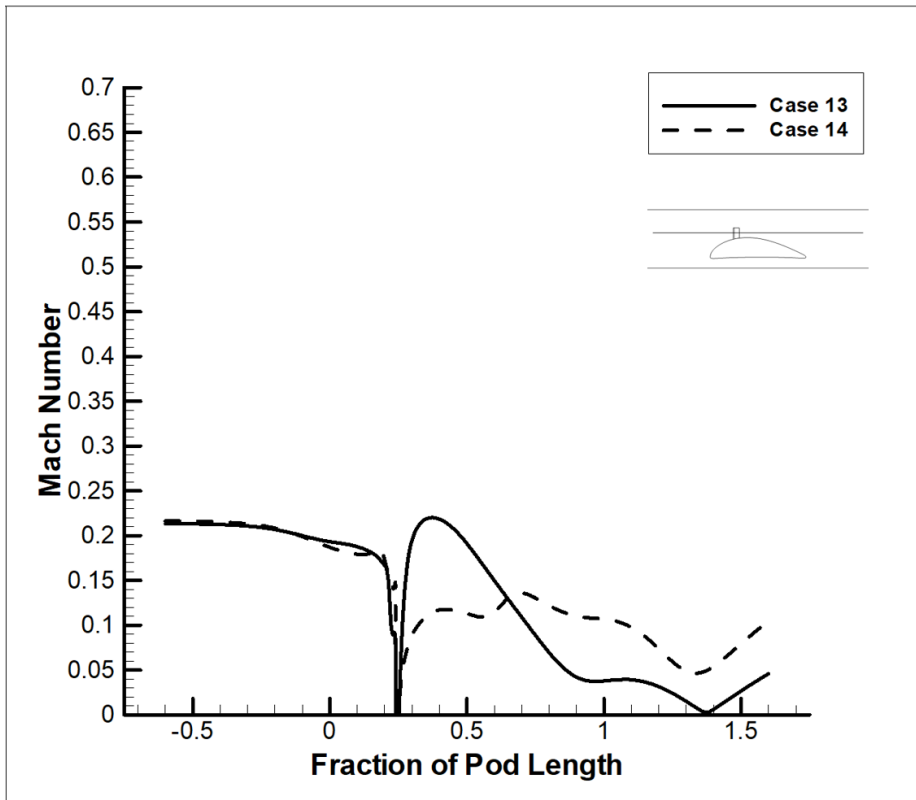


Figure 4.22. Mach number distribution along line 2 for cases 13-14

The first thing to notice about line 2 is that in all cases, the Mach number drops to 0 at 0.24 chord. This is due to the presence of the brake plate. There are also fluctuations and rise to a higher-than-initial Mach number in the wake region of the brake for all cases, with the maximum Mach number occurring for case 12. For constant brake length, larger fluctuation in Mach number is observed for forward facing brakes than backward facing ones.

The geometry of the pod is also observed to affect the flow field even before it encounters the leading edge of the pod. Between cases 1 through 4 (constant brake length with increasing angle of attack), the initial Mach number at the leading edge of the pod rose from 0.2 to 0.265. Peak Mach numbers are also observed to increase from case 1 to case 4, with the peak Mach being 0.05 and 0.2 for case 4. It is also observed that the Mach variation in wake region increases from case 1 to 4, i.e. Mach fluctuation increases as the brake plate is oriented further away from the fluid flow. This may be due to decrease of brake profile with angle variation, and thus the subsequent decrease in cross sectional area of wake region perpendicular to the fluid flow.

While the same observations are observed in the forward-facing cases, the effect is more significant. Initial Mach values increase with increase in angle of attack, with case 5 having values at 0.21 Ma while case 8 begins at 0.29 Ma. Slight increase in Mach number is also observed as the flow encounters the leading edge, with the effect being most prominent in case 8, where value initially dips to 0.25 Ma at the leading edge before rising back to 0.27 Ma immediately before the brake plate. The peak Mach numbers in the wake region are greater for forward-facing brake than backward-facing, with case 5 having peak value of 0.22 Ma, while case 8 reaches as high as 0.47 Ma. It is noteworthy that the lowest peak Ma for forward-facing brake plate of constant length occurs for case 6, at only 0.18 Ma, seemingly against the trend of increased Mach numbers with increased angle of attacks. It should also be noted that Mach fluctuation in the wake region decreases with increase in attack angle.

Initial Mach numbers of approach for backward-facing constant profile brakes are larger than for constant plate cases. The values increase from 0.2 Ma for case 9 to 0.25 for case 12. There is also a significant rise in Mach number for each case, with the case again being prominent at high angle of attack, the Mach number for case 12 rising

from 0.25 Ma to 0.3 Ma at the leading edge. With the exception of case 9, all geometries achieve higher Mach number in the wake region than during approach, and the peak values also increase with increase in angle of attack. The peaks also occur at earlier points as angle of attack is increased, with case 10 reaching 0.3 Ma near the trailing edge while case 12 reaches 0.51 Ma at the halfway point of the pod.

For forward facing cases, the initial Mach of approach is more or less equal at 0.21 Ma. The variation in Mach is the lowest in these cases, with the peak for case 13 being at 0.22 Ma and that for case 14 being at approach, with the flow only reaching a peak of 0.11 Ma in the wake region. Case 13 is of particular interest as the Ma rises very steeply after the brake and falls quickly as well, being less than 0.05 Ma at the trailing edge. The flow is also observed to completely stop in the region behind the pod, perhaps indicating greater vorticity effects.

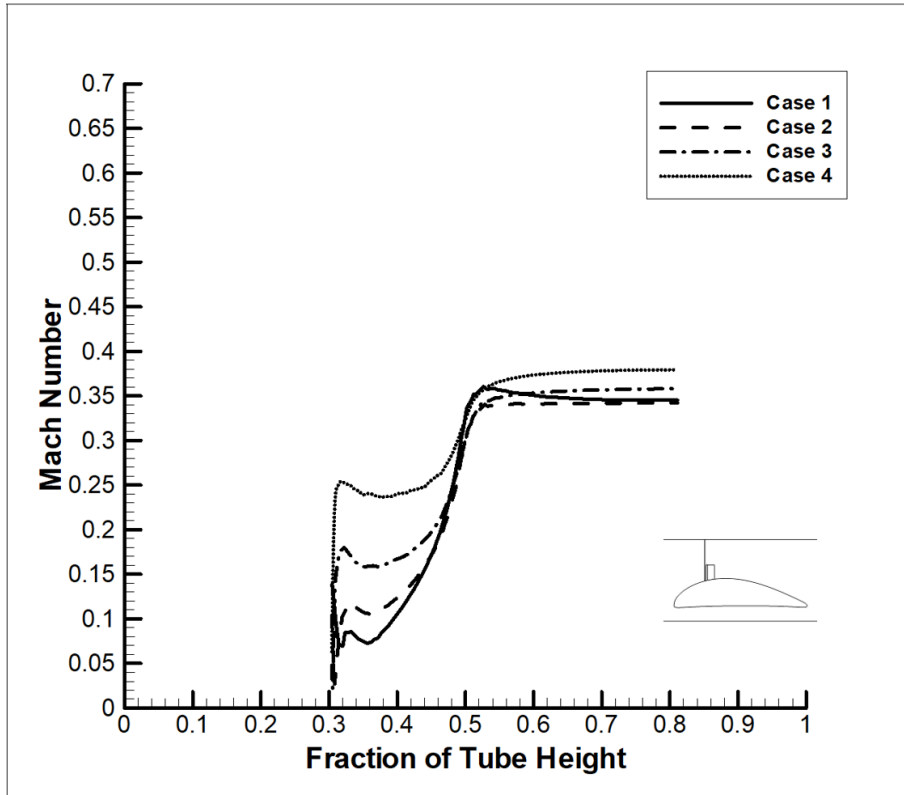


Figure 4.23. Mach number distribution along line 3 for cases 1-4

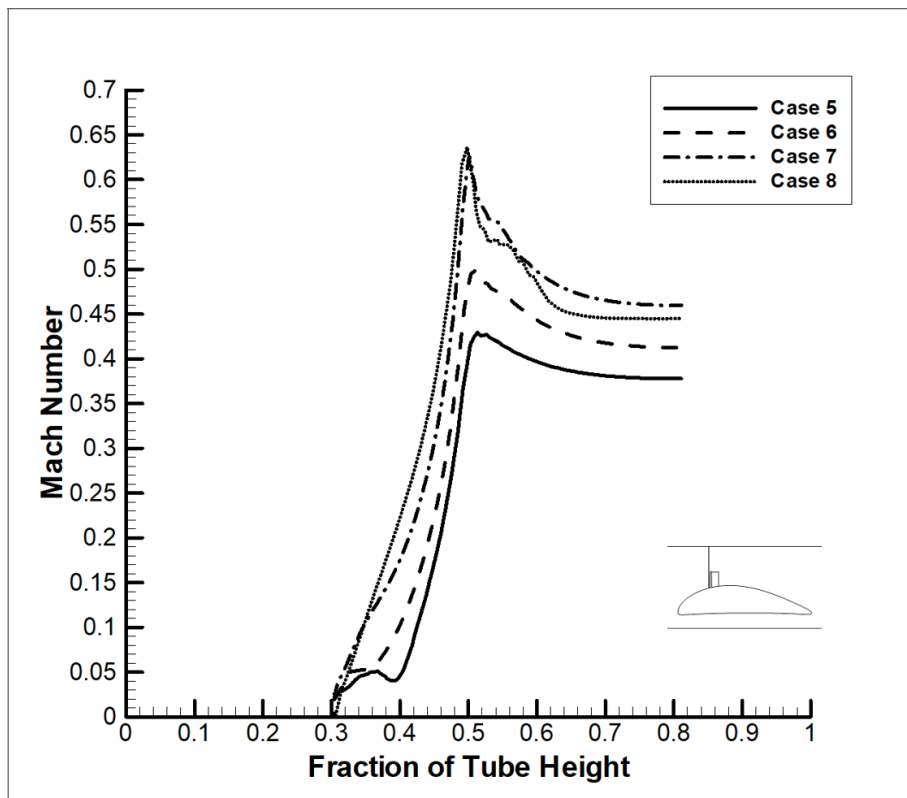


Figure 4.24. Mach number distribution along line 3 for cases 5-8

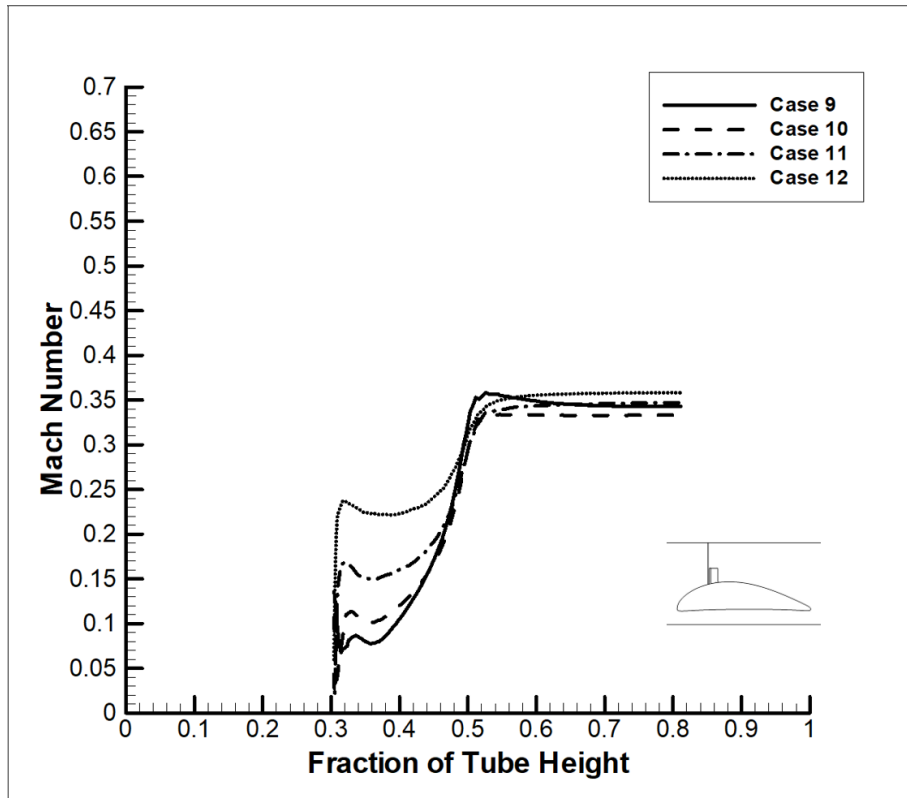


Figure 4.25. Mach number distribution along line 3 for cases 9-12

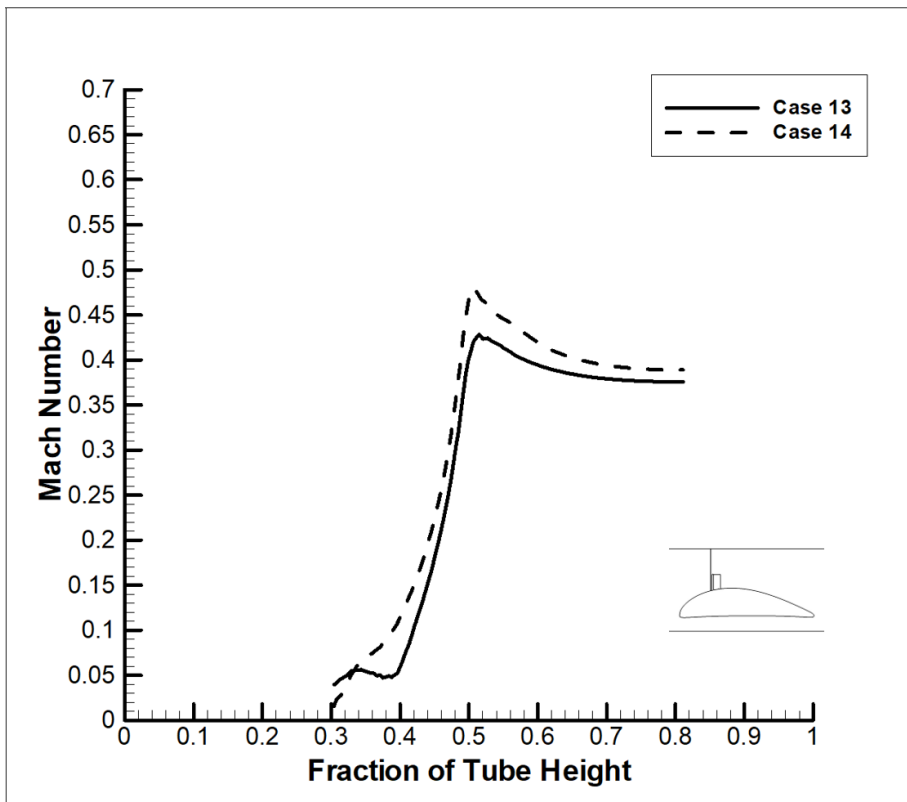


Figure 4.26. Mach number distribution along line 3 for cases 13-14

Line 3 figures show the variation of the Ma with height of pod, i.e how the flow changes at pod surface and above immediately in front of the brake plate. For cases 1 through 4, having backward facing brake at constant brake plate length, we see that the Ma value at the pod surface is low, but increases as angle of attack increases, as brake force decreases and thus flow is less decelerated as angle increases. The Mach number is seen to fall across the height of the plate and then rise steeply to a stable peak value above the brake. The range of peak values is comparatively small, with case 2 having the minimum Ma value of 0.33 Ma, and case 1 having value 0.36 Ma. It should be noted that case 1 initially peaks at 0.36 Ma before falling to stable value 0.34 Ma, whereas others stabilize at 0.33 Ma. Cases 9 through 12, i.e backward facing brakes with constant profile lengths, follow the same trends with the stable values occurring in closer range, case 10 having minimum value at 0.33 Ma, and case 9 having maximum value at 0.34 Ma. Similar to case 1, case 9 reaches peak at 0.35 Ma before stabilizing at 0.34 Ma, while cases 10,11, and 12 stabilize at the peak value.

For case 5 through 8, having forward facing brakes at constant brake plate length, a steep rise in Mach number is observed as height increase along the brake, with the gradient of the rise and the peak values increasing with increase in angle of attack. The Ma then falls with increase in height and ultimately reaches a stable value above the brake plate. The stable values above the brake are observed to increase with increase in angle of attack, with case 5 having the lowest value at 0.38 Ma, and case 8 having the largest value at 0.46 Ma. Erratic flow patterns are observed for case 8 as flow decelerates above brake plate from peak value. it can thus be concluded that the decrease in drag force on the brake with increase in angle leads to less flow deceleration above the pod, and thus higher Mach numbers being observed. Similar trends are observed for case 13 and 14, with peak values occurring for case 13 and 14, at 0.42 Ma and 0.47 Ma respectively, and stable values occurring at 0.37 Ma and 0.38 Ma for cases 13 and 14 respectively.

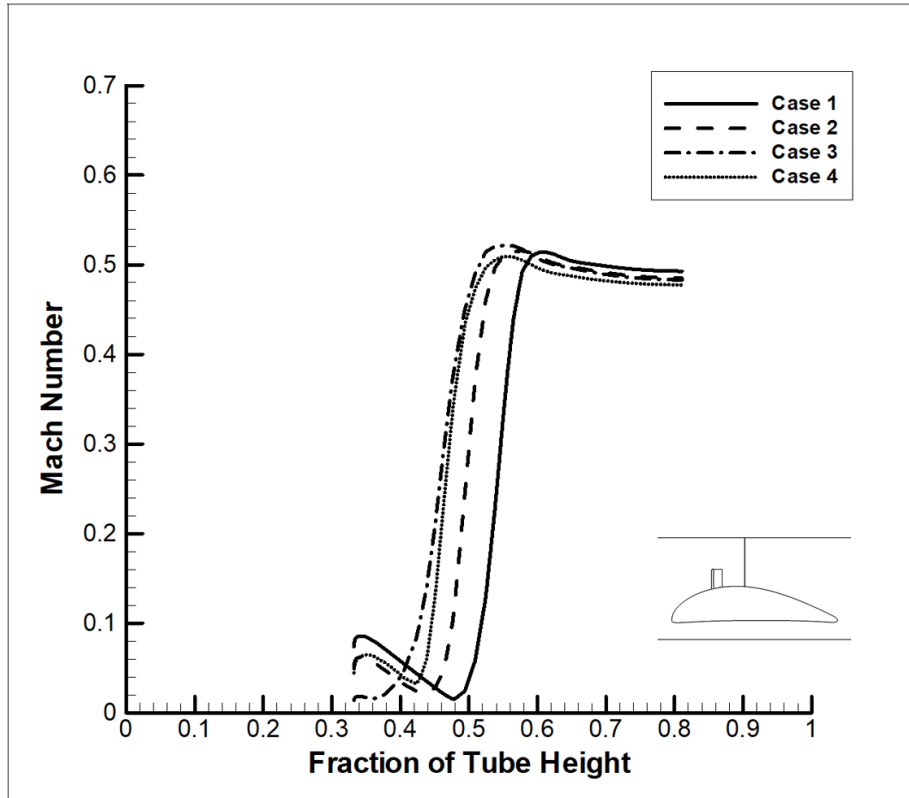


Figure 4.27. Mach number distribution along line 4 for cases 1-4

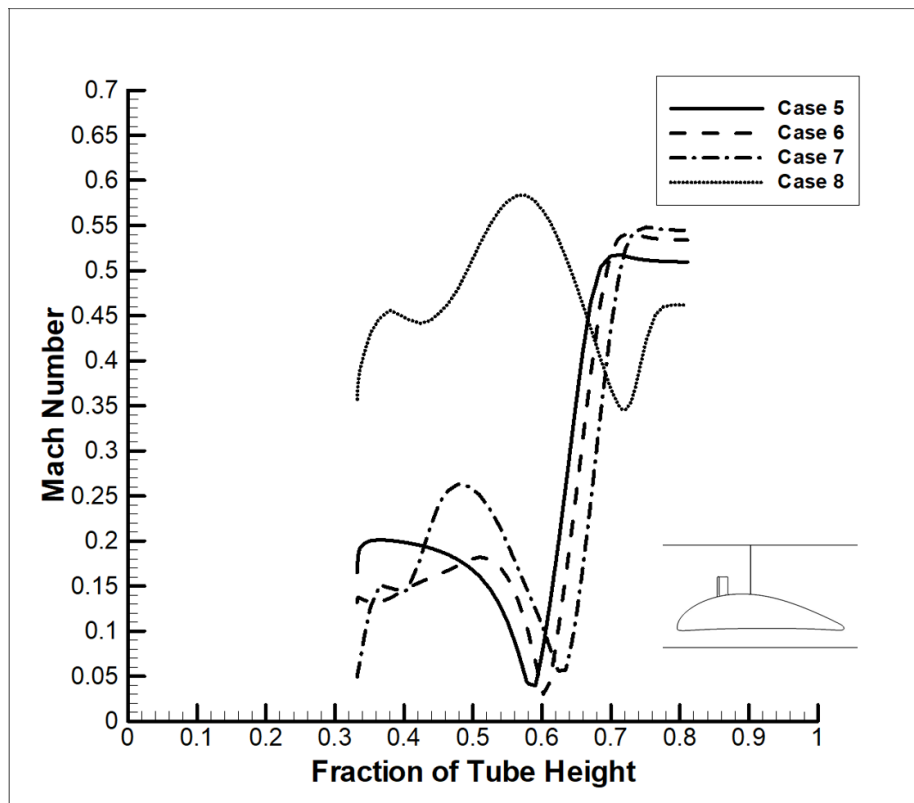


Figure 4.28. Mach number distribution along line 4 for cases 5-8

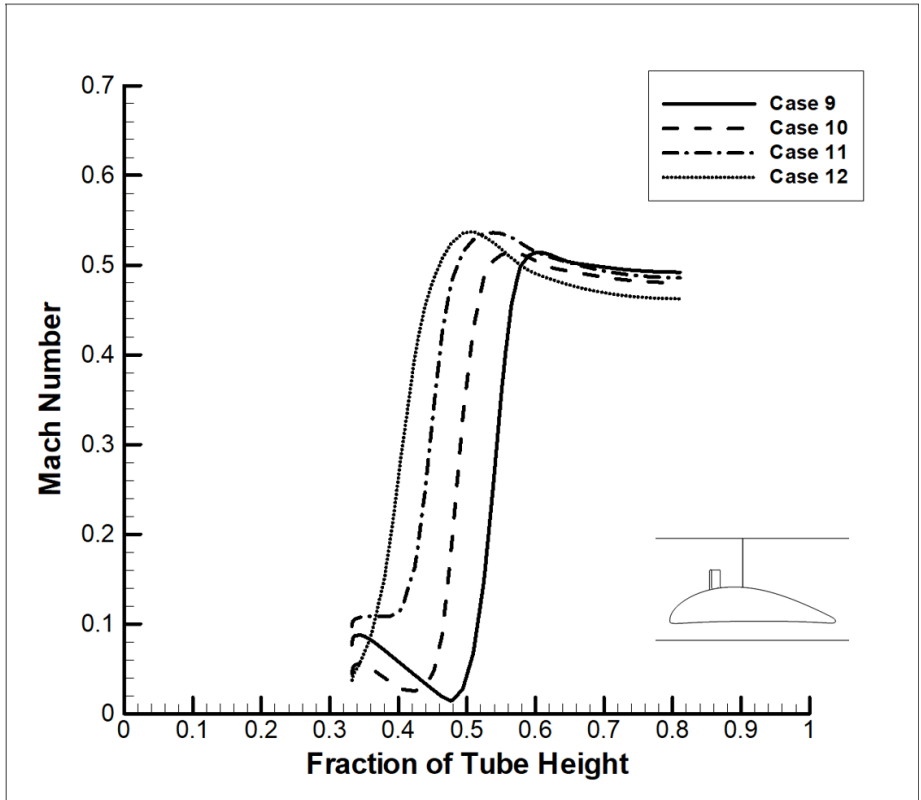


Figure 4.29. Mach number distribution along line 4 for cases 9-12

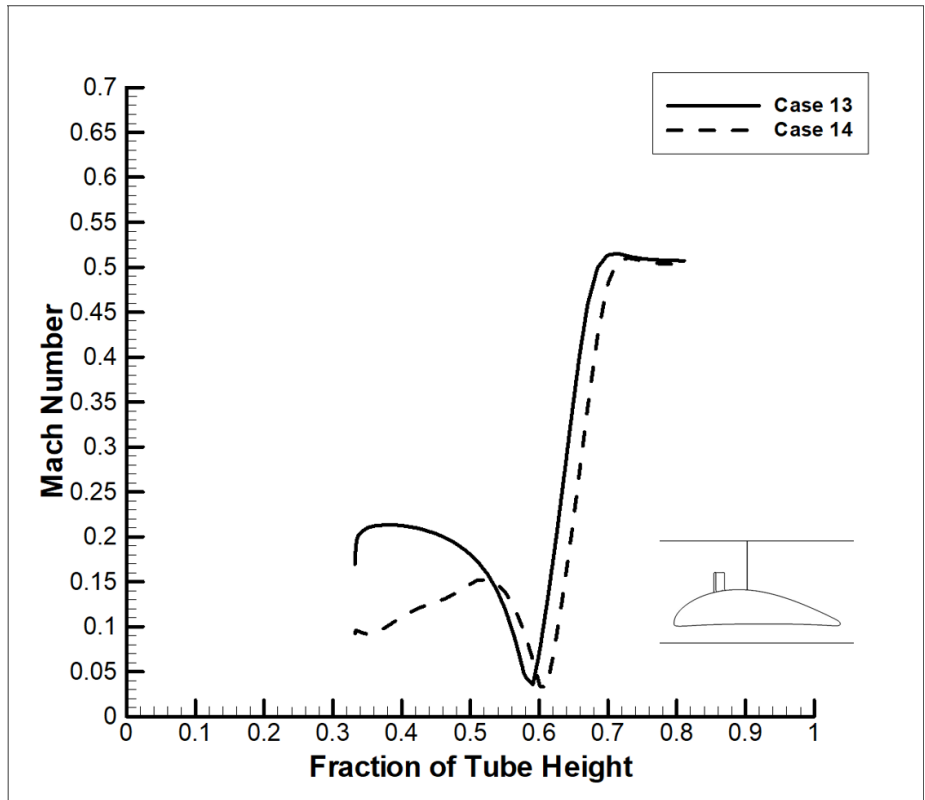


Figure 4.30. Mach number distribution along line 4 for cases 13-14

For cases 1 through 4, the Mach number is seen to fall across the height of the wake region behind the brake. However, above the brake, as the flow region reconciles, the Mach number increases with large gradient before reaching the peak value and stabilizing. The peak values vary through a small range of 0.01 Ma, with case 1 peaking at 0.51 Ma, and case 3 at 0.52 Ma. In all four cases, the flow is stable at a lower Mach number than the peak, with the range of stable values being small as well, case 1 stabilizing at 0.49 Ma and 0.47 Ma. The noticeable trends are that the flow reaches peak velocity, i.e. reconciles earlier, and at higher speeds, with increase in angle of attack, and that the stable Mach values above the pod decrease with increase in angle of attack. Mach number at pod surface is also seen to decrease with increase in angle of attack. We can thus conclude that for the backward facing plate having constant brake plate length, similar to flow in front of the brake plate, the flow acceleration above the pod is larger with increase in attack angle, as flow is less decelerated by presence of brake plate and thus reconciles faster.

For cases 5 through 7, the overall trend observed is that Mach number decreases across the height of the brake plate, before increases steeply to peak values and stabilizing at the peak value. The Mach number at the surface of pod is seen to decrease with increase in angle of attack. However, with increase in angle of attack, the fluctuation during pressure fall increases, as the flow in the wake region becomes more erratic. Similar to case 1 through 4, as the angle of attack increases, the minimum Ma is reached at earlier fractions, and correspondingly the peaks are also reached earlier. The peak values also increase with increase in angle of attack, although the range of values is small; case 5 peaking at 0.5 Ma and case 7 at 0.55 Ma. Of particular note is the overall decrease in Mach number across the height of the brake plate as the angle of attack increases. Cases 13 through 14 show the same trends, however with decreased peak values. The peak for case 14 occurs at a later stage than for case 13, and is slightly lower. However, both cases produce almost identical curves after stabilizing at peak value of 0.5 Ma.

Case 8 shows the most erratic behavior, with high Mach value at pod surface, 0.36 Ma, before rising across the height of the brake plate, to a peak value of 0.57 Ma, falling steeply to 0.35 Ma at 0.7 height fraction, and then rising again and stabilizing at 0.45 Ma.

Case 9 through 12 show similar trends to cases 1 through 4, with the effects becoming more prominent for constant brake profile cases. The peaks occur at earlier fractions of the height, moving back about 0.06 fractions of the height with each increment in angle of attack. The peak values of Mach number also increase with increase in angle of attack, being 0.51 Ma for case 9 and 0.53 Ma for case 12, with the stable values decreasing with increase in angle of attack, case 9 having stable value of 0.49 Ma, and case 12 having 0.56 Ma.

The following figure has been drawn up for case 9 to help visualize the flow better –

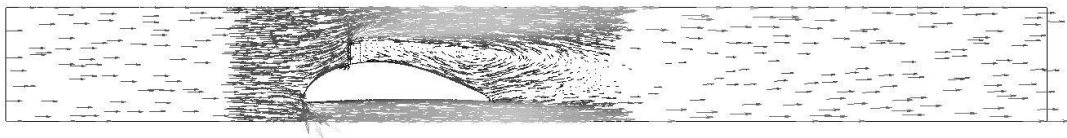


Figure 4.31. Flow vector

As the flow approaches the pod, it encounters a shock at the leading edge. The pressure at this point is a stagnation pressure and the Mach number here is zero. The flow gets diverted in two directions, over and below the pod, as seen from figure 4.31. The flow below the pod experiences a sudden increase in speed due to the sudden reduction in flow area whereas the flow over the pod speeds up slightly up to the brake plate [figure 4.33]. The flow over the brake suddenly speeds up, again due to the sudden reduction in flow area. Both these flows over and below the pod merge further downstream. The Mach number reaches its initial value close to the outlet of the tube. As the flow decelerates at the downstream due to continuity, the pressure again increases according to Bernoulli's principle.

An adverse pressure gradient occurs just behind the brake plate. The pressure behind the brake is lower than the pressure further downstream. Thus, a reverse flow occurs at this section. This flow, combining with the high-speed flow over the brake plate, results in a circulatory motion behind the brake. This region is known as the recirculation region and is responsible for acting against the drag.

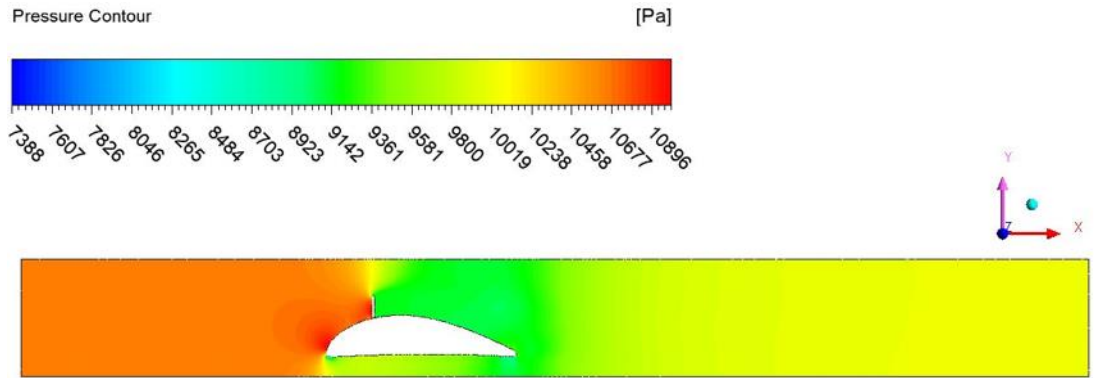


Figure 4.32. Pressure contour

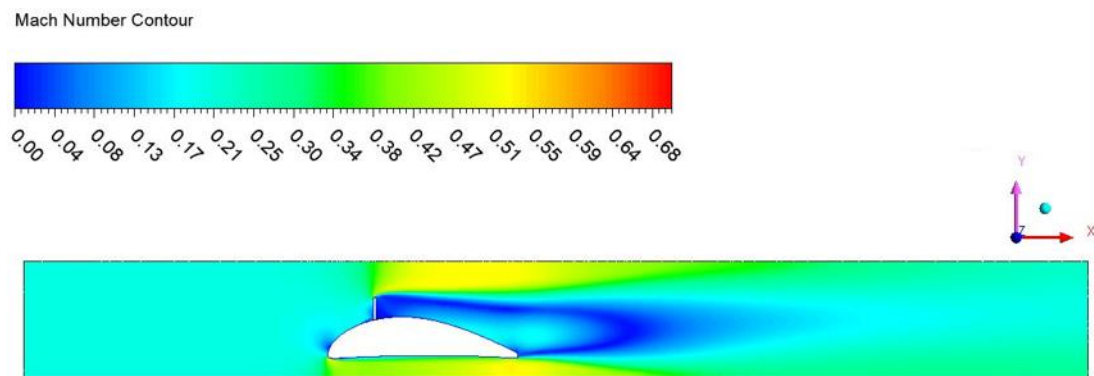


Figure 4.33. Mach number contour

The pressure contour shows that since the brake plate hinders the flow of air around the annulus region, a pressure build-up occurs in front of the pod. Also, the pressure below the pod is slightly higher than that on top of the pod behind the brake plate. This suggests that the pod experiences a lift force.

The deployed angled brake will also be likely to cause two moments on the pod –

- 1) The component of the drag force perpendicular to the vertical distance of the brake would result in an overturning moment of the pod in the clockwise direction about the positive z-axis.
- 2) The component of the drag force perpendicular to the horizontal distance of the brake would result in a turning moment of the pod in the clockwise direction about the positive y-axis.

Chapter 5

Results for Multiple or Split Brakes

As discussed in the previous section, this approach involved multiple brake plates being used at different positions of the pod in various ways to try to maximize the total drag force. Three different cases were studied –

- 1) Three brakes of equal length
- 2) Two brakes of different length
- 3) Two brakes of equal length

5.1 Three Brakes of Equal Length

The three brake plates created multiple recirculation regions in the flow field but of much lower intensity compared to the previous case. The drag forces on the pod and the brake plates were of the following manner –

Part	Drag Force (N)
POD	413.46
BRAKE 1 (Front)	86.98
BRAKE 2 (Middle)	-6.12
BRAKE 3 (Rear)	9.86
Total	504.18

An interesting thing to notice about this result is that the force on the 2nd brake plate is negative, which means that the resultant of the backward drag and the forward reverse flow is in the forward direction. The reverse flow on this brake is stronger than the drag. The other two brake plates also produced small amounts of drag. The total drag on this geometry sums up at 504.18 N, much less than the previous cases.

The flow is better visualized by the following images –

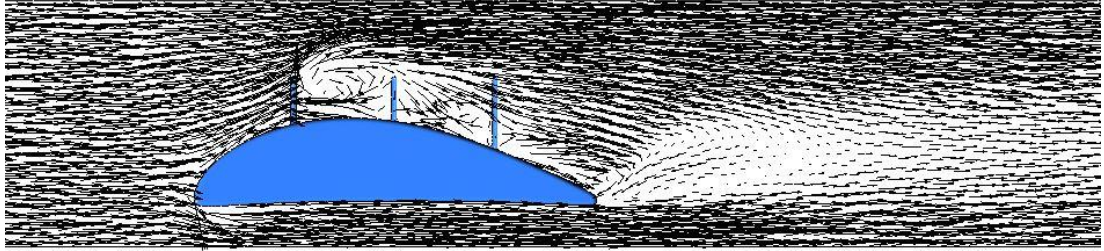


Figure 5.1. Flow vector of Case 15

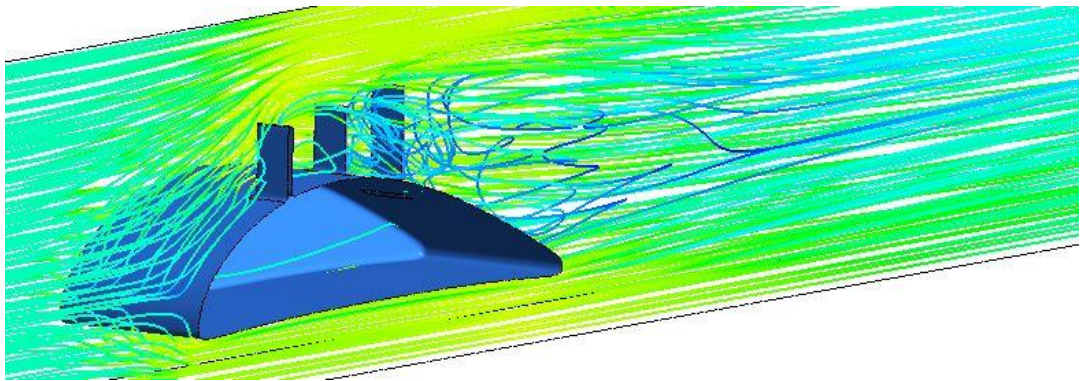


Figure 5.2. Flow streamline of Case 15

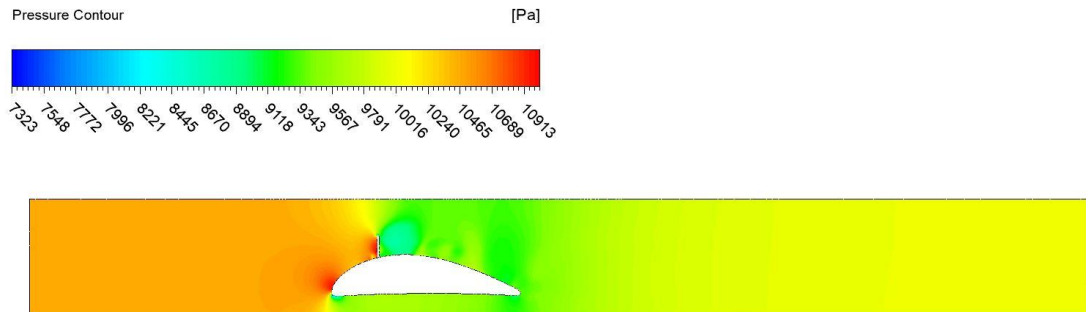


Figure 5.3. Pressure contour of Case 15

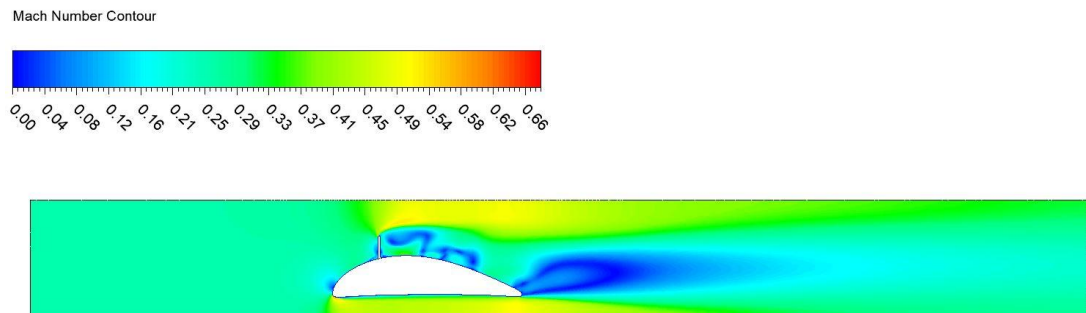


Figure 5.4. Mach number contour of Case 15

5.2 Two Brakes of Different Length

The rear brake on this geometry failed to produce a significant drag in spite of having a large surface area. The reason is that as the flow converges at the front section of the pod, it has a linear velocity tangent to the pod's surface, which is angled slightly upward. As a result, most of the flow passes up and over the rear brake plate, making it ineffective. A small vortex is also created behind the front brake plate.

The forces found are –

Part	Drag Force (N)
POD	495.95
BRAKE 1 (Front)	72.03
BRAKE 2 (Rear)	29.53
Total	597.51

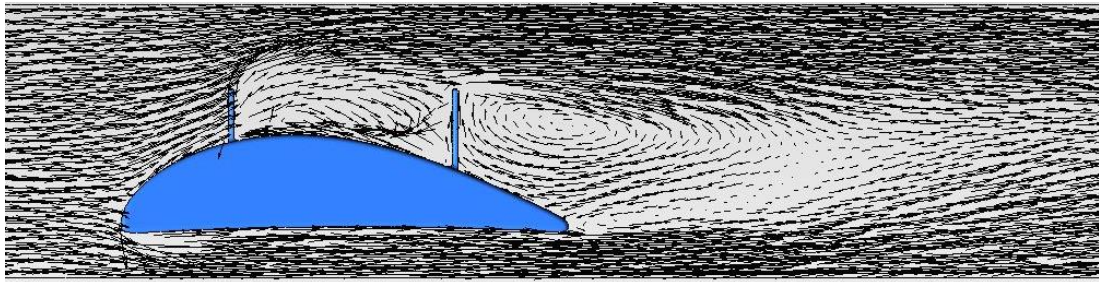


Figure 5.5. Flow vector of Case 16

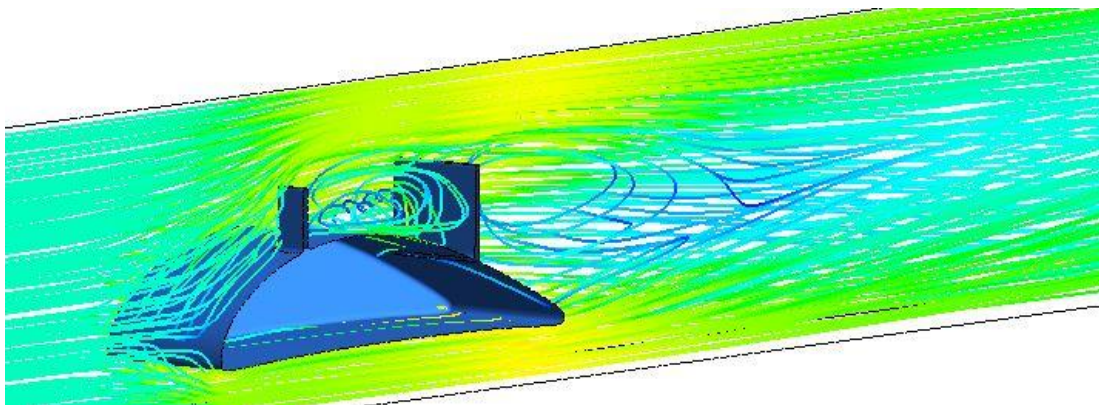


Figure 5.6. Flow streamline of Case 16

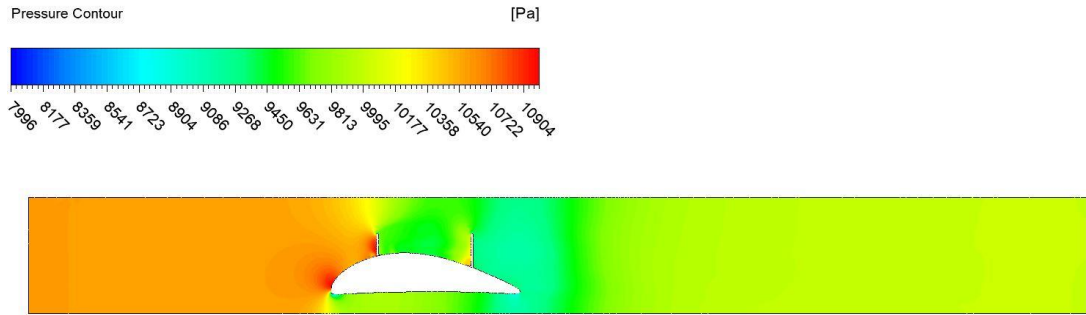


Figure 5.7. Pressure contour of Case 16

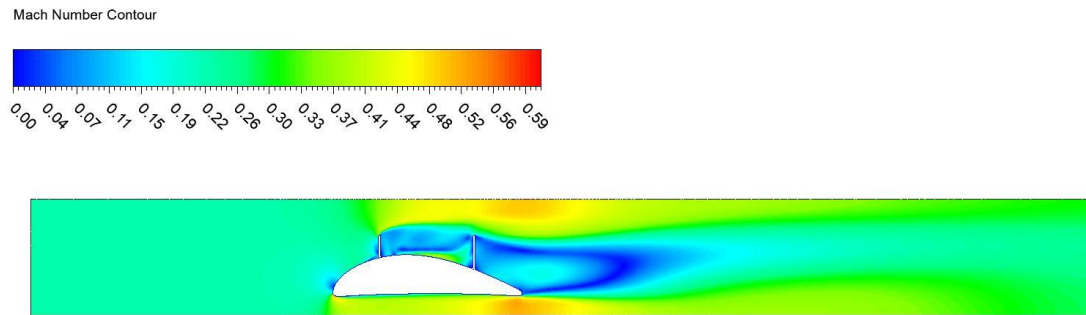


Figure 5.8. Mach number contour of Case 16

5.3 Two Brakes of Equal Length

Since the front brake plate was situated just behind the extreme front of the pod, it encountered the maximum amount of normal flow and hence, produced the greater drag. Due to this brake, a very small vortex region was created in front of the rear brake plate. Also, after diverting off the front plate, some of the flow went up and over the rear plate. These two effects caused the drag on the rear plate to significantly drop.

The forces found are -

Part	Drag Force (N)
POD	-88.92
FRONT BRAKE	463.14
REAR BRAKE	255.8
Total	630.02

The cause of the negative force on the pod could be the huge recirculation region behind the rear brake plate, as seen in the following images.

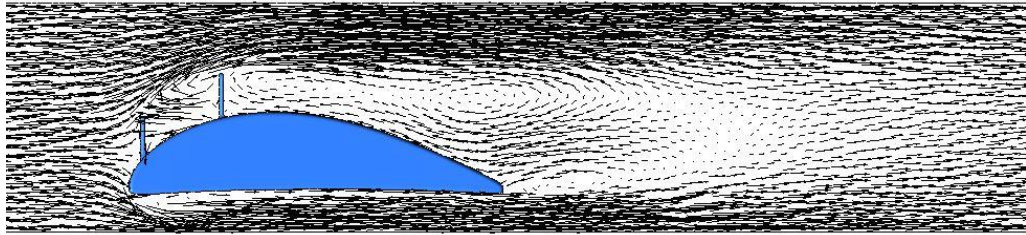


Figure 5.9. Flow vector of Case 17

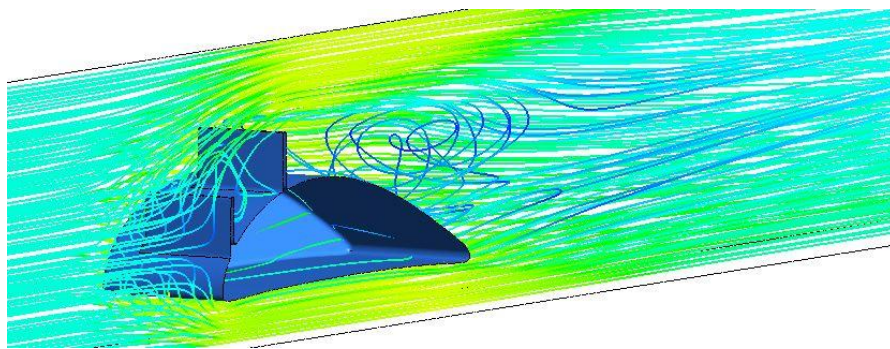


Figure 5.10. Flow streamline of Case 17

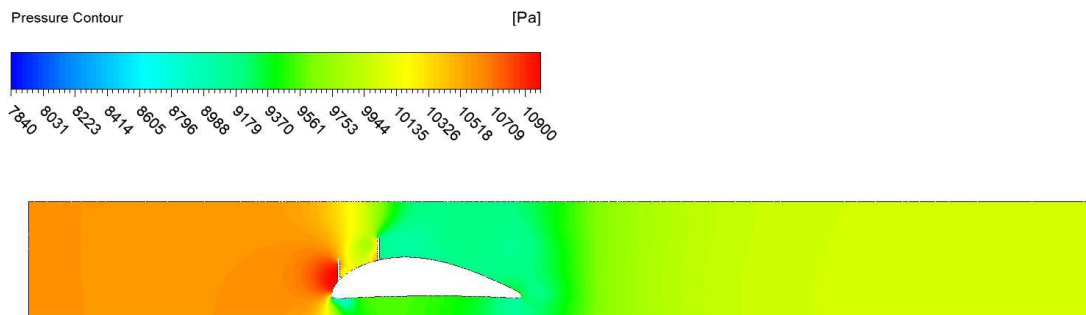


Figure 5.11. Pressure contour of Case 17

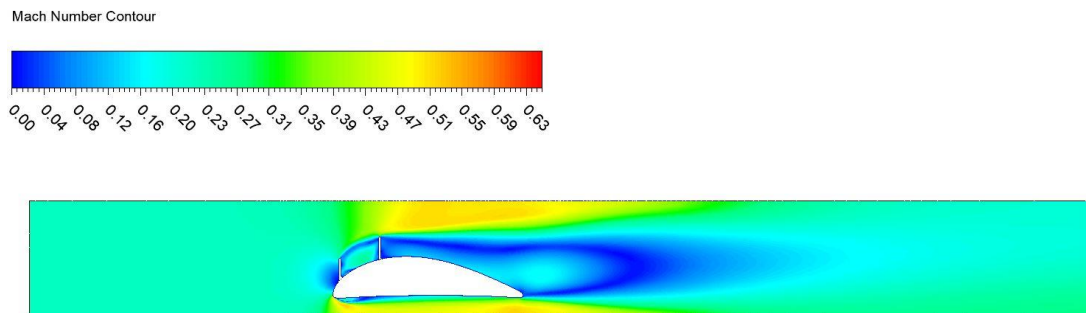


Figure 5.12. Mach number contour of Case 17


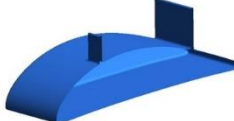
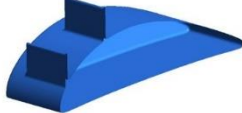
Case	Geometry		Total Drag Force (N)
15	Three brakes of equal length		504.18
16	Two brakes of different lengths		597.51
17	Two brakes of equal length		630.02

Figure 5.13. Summary results of Multiple or Split Brakes

Chapter 6

Conclusions and Scope of Further Work

The inclusion of the aerodynamic flat brake plate gives rise to a substantial amount of drag force that can lower the braking power and the electricity consumption of the magnetic braking system deployed on the pod track. Drag is directly proportional to the square of the velocity. The actual Hyperloop is stated to travel at speeds close to Mach 1.0 and at these transonic levels, the drag force will be immense and the aerodynamic flat brake plate will play a significant role on the behavior of the pod. Alongside the positives, the flow complexities increase as higher speeds are reached, and the complications warrant further study. There is scope of carrying out further research in relation to this topic.

- Till now, studies have been limited to steady-state analysis. The actual Hyperloop is not expected to maintain constant speeds throughout its journey. A transient analysis of the pod as it moves through the tube is recommended.
- How will the aerodynamic flat brake plate and the pod surface behave in response to the greater amount of drag? The model has been assumed to be structurally stable but it is necessary to study how far the structural integrity will hold. A stress analysis of the geometry is subject to further studies.
- This paper deals with the flow characteristics and behavior of the aerodynamic flat brake plate on the base pod design put forward by Braun and adds on the studies of Saniat and Raihan [28]. The actual Hyperloop does not have one universal design. The pods showcased in the SpaceX Hyperloop Pod Competition have encompassed a multitude of designs and the pod designs revealed by commercial companies like Virgin Hyperloop One and Hyperloop Transportation Technologies have been varied. How the aerodynamic flat brake plate and the other design angles, and the design features will perform on the different pod geometries are subject to further studies.
- The study on the performance of the slotted pod has been limited and there remains scope on further work on the number of inlet and outlet panels, the behavior of the flow through the slot, optimization of the slot width, the

placement of the panels and the optimum results of coupling the slot with the aerodynamic flat brake plate.

- A 3D printed scaled down version of the model can be analyzed in a wind tunnel and the results of this experimental method can be compared with the numerical solution.
- The pod can have a slot that opens up at the leading edge, runs around the pod wall and exits at the trailing edge. The slot can be 40 mm wide for the scaled down model. During travel, air at the pod leading edge will flow through the slot. The drag forces are expected to be reduced and this can help in acceleration. The slot will remain closed during braking.

Bibliography

- [1] E. Musk, "Hyperloop alpha", SpaceX Retrieved August 13 2013
- [2] J. Braun, J. Sousa, C. Pekardan, "Aerodynamic Design and Analysis of the Hyperloop", Purdue University, West Lafayette, Indiana 47906, AIAA Journal
- [3] M.M.J. Opgenoord, P.C. Caplan, "Aerodynamic Design of the Hyperloop Concept", Massachusetts Institute of Technology, Cambridge, MA, 02139
- [4] J.C.Chin, J.S.Gray, S.M.Jones, J.J.Berton, "Open-Source Conceptual Sizing Model for the Hyperloop Passenger Pod", NASA Glenn Research Center, Cleveland, OH, 56th American Institute of Aeronautics and Astronautics (AIAA)/ASCE/ASH/ASC Structures, Structural Dynamics and Materials Conference January 2015
- [5] X. Chen, L. Zhao, J. Ma, Y. Liu, "Aerodynamic Simulation of evacuated tube maglev trains with different streamline designs", Journal of Modern Transportation, Volume 20, Number 2, June 2012, Page 115-120
- [6] M. Woelke, "Eddy Viscosity Turbulence Models employed by Computational Fluid Dynamics", Transactions of the Institute of Aviation No. 191
- [7] M. Puharic, D. Matic, S. Linic, S. Ristic, V. Lucanin, "Determination of Braking Force on the Aerodynamic Brake by Numerical Simulations", FME Transactions, Volume 42, Number 2, Page 106-111
- [8] I. Vasovic, M. Maksimovic, M. Puharic, D. Matic, S. Linic, "Structural Analysis of Aerodynamic Brakes in High-Speed Trains", Scientific Technical Review, 2011, Vol.61, No.2, Page 10-15
- [9] F. R. Menter, "Improved two-equation k-turbulence models for aerodynamic flows" NASA technical memorandum 103975, no. 1 (1992)
- [10] Y. A. Cengel, J. M. Cimbala, *Fluid Mechanics: Fundamentals and Applications*, 3rd edition, McGraw-Hill
- [11] Y. A. Cengel, A. J. Ghajar, *Heat and Mass Transfer: Fundamentals and Applications*, 5th edition, McGraw-Hill
- [12] J. Tu, G. H. Yeoh, C. Liu, *Computational Fluid Dynamics: A Practical Approach*, 2nd edition, Butterworth-Heinemann

- [13] J. D. Anderson Jr, *Fundamentals of aerodynamics*, Tata McGraw-Hill Education, 2010
- [14] G. A. Bird, *Molecular Gas Dynamics*, NASATR A76, 1976
- [15] J. D. Anderson Jr, *Computational Fluid Dynamics: The Basics with Applications*, International Edition 1995, McGraw-Hill
- [16] H. K. Versteeg, W. Malalasekera, *An Introduction to Computational Fluid Dynamics: The Finite Volume Method*, 2nd edition, Pearson Education Limited
- [17] SpaceX Hyperloop Test Track Specification, Revision 5.0, February 2016
- [18] MIT Hyperloop Final Report, August 2017
- [19] <https://www.spacex.com/hyperloop>
- [20] <https://www.theverge.com/2018/7/22/17601280/warr-hyperloop-pod-competition-spacex-elon-musk>
- [21] <https://www.theverge.com/2019/7/22/20703423/tum-hyperloop-record-463-kmph-spacex-elon-musk-competition>
- [22] <https://www.teslarati.com/spacex-2018-hyperloop-success-celebration-2019-registration-opened/>
- [23] M. Puharić, V. Lučanin, S. Ristić, S. Linić, “Application Of The Aerodynamical Brakes On Trains”, *Research And Design In Commerce & Industry*, Issn 1451-4117, Udc 33, 8(2010)1, 2010,168, Pages 13-21
- [24] <https://www.hyperloop.global/about>
- [25] <https://hyperloop-one.com>
- [26] Z. Jianyong, W. Mengling, T. Chun, X. Ying, L. Zhuojun, C. Zhongkai, “Aerodynamic braking device for high-speed trains: Design, simulation and experiment”, *Proceedings of the Institution of Mechanical Engineers, Part F: Journal of Rail and Rapid Transit* 2014 228: 260 DOI: 10.1177/0954409712471620
- [27] M. Yoshimura, S. Saito, S. Hosoka, H. Tsunoda, “Characteristic of the Aerodynamic Brake of the Vehicle on the Yamanashi MAGLEV Test Line”, *QR of RTRI*, Volume 41, No. 2, June 2000
- [28] T. S. Saniat and M. R. Uddin, “Feasibility analysis of an aerodynamic braking system for the Hyperloop Transport Pod in low pressure, high Mach flow regime”, IUT, 2018

- [29] <https://www.computationalfluiddynamics.com.au/tips-tricks-cfd-estimate-first-cell-height/>
- [30] F. M. White, *Fluid Mechanics*, 5th edition, McGraw-Hill
- [31] N. Riva, L. Benedetti, Z. Sajó, “Modeling The Hyperloop With COMSOL Multiphysics®: On The Aerodynamics Design Of The EPFLoop Capsule”